MICROSEISMIC VELOCITY INVERSION AND EVENT LOCATION USING REVERSE TIME IMAGING

by

Ashley M. Fish

A thesis submitted to the Faculty and the Board of Trustees of the Colorado School of Mines in partial fulfillment of the requirements for the degree of Masters of Science (Geophysics).

Golden, Colorado

Date _____

Signed: _____
Ashley M. Fish

Approved: _____
Dr. Paul Sava
Associate Professor of Geophysics
Thesis Advisor

Golden, Colorado

Date _____

_____
Dr. Terence K. Young
Professor and Head,
Department of Geophysics

ABSTRACT

Microseismic monitoring is an essential tool in the oil and gas industry because it is a widely used measurement which characterizes hydraulic fracture reservoir completions. High pressure fluid injection causes stress changes in the target formation thus reactivating pre-existing fracture networks. To characterize the reactivated fracture networks, or stimulated reservoir volume (SRV), most assume that the microseismic event hypocenters are a direct indicator of the size and orientation of the paths of fluid flow within the reservoir. Accordingly, without correctly locating and characterizing microseismic events, operators cannot attempt to model or assess the stimulated reservoir. Current acquisition and processing techniques do not yet provide the consistency and repeatability needed to accurately locate microseismic events, let alone characterize the SRV. I challenge the use of conventional ray-based techniques and advocate the use of wavefield-based methods as a more accurate and more robust alternative. Wavefield-based methods are capable, in principle, to focus microseismic energy at its source position and at its trigger time even when data are corrupted by high levels of noise. However, this relies on a good understanding of the models used for wave propagation, a known source onset-time, as well as a broad acquisition aperture. I explore the benefits and pitfalls associated with wavefield-based methods and emphasize the need for wide aperture in microseismic acquisition. Extending these techniques into velocity model updating, I advocate the use of Waveform Tomography, both in the data- and image-domain, to produce a high resolution velocity model. A better constrained model produces more reliable event locations. I also emphasize the need for routine recording of perforation shot onset timing which is required by wavefield tomography.

TABLE OF CONTENTS

ABSTRACT iii

LIST OF FIGURES vi

ACKNOWLEDGMENTS ix

Chapter 1 INTRODUCTION 1

Chapter 2 APERTURE EFFECTS ON WAVEFIELD FOCUSING 7

2.1 Introduction 7
2.2 Effects of Aperture on Focusing 17
2.2.1 Theoretical Array Geometries 17
2.2.2 Case Study Array Geometries 26
2.3 Conclusions 34

Chapter 3 FINDING THE SOURCE ONSET TIME 35

3.1 Introduction 35
3.2 Finding the source onset time: a synthetic example 37
3.3 Finding the source onset time: a field example 45
3.4 Conclusions 52

Chapter 4 EFFECTS OF INCORRECT VELOCITY ON WAVEFIELD FOCUSING 53

4.1 Introduction 53
4.2 Effects of Incorrect Velocity on Wavefield Focusing 54
4.2.1 Case Study 54
4.3 Methods for Updating the Velocity Model 60
4.3.1 Waveform Tomography: data-domain 61
4.3.2 Waveform Tomography: image-domain 66
4.4 Conclusions 70

Chapter 5 CONCLUSIONS AND FUTURE WORK 71

5.1 Conclusions 71
5.2 Suggested Future Work 72

REFERENCES 75

APPENDIX A 77

A.1 Local Earthquake Tomography 77

APPENDIX B 81

B.1 Backus Averaging 81
B.1.1 Well Log Upscaling Methodology 82
B.1.2 Case Study Results 84

LIST OF FIGURES

2.1 A simple cartoon illustrating a three-dimensional slice in the wavefield around the source location (e.g., A perforation shot in the examples to follow). The top left panel is the $x-t$ plane of the wavefield in space and time, the bottom left panel is the $x-z$ plane in space, and the bottom right panel is the $z-t$ plane in space and time. The axes of the panels are the change in space and time with respect to the absolute position of the source location. The change in space and time is measured in km and ms, respectively. 9

2.2 A poor aperture (top) defocuses the microseismic event, whereas a full-aperture (bottom) provides the best resolution of the focus. 12

2.3 Case study: dual borehole array (receivers located in the monitor wells at $x = 0.88$ km and $x = 1.47$ km), 20 perforation shots (located at $z = 2.67$ km), and the sonic velocity log used to produce the 2D velocity model (overlaid on right). Velocity values range from 4.63 km/s in dark grey to 5.86 km/s in white. 13

2.4 Case study: well logs. From left to right: gamma ray (GR), fractional porosity, density, compressional velocity, and 150 Hz wavelet. 15

2.5 Raw, unfiltered perforation shot data used to image the known shot locations. The field data are three-component and elastic in nature. To simplify, I use a single horizontal component of the field data in the simulations and I assume an acoustic medium. 16

2.6 Full-aperture array and velocity model. The receiver array (box) is dense and surrounds a single source located at $x = 1.17$ km and $z = 2.38$ km. . . . 17

2.7 Focusing due to a full-aperture box array surrounding the source. The focal point, as expected, resides at the cross-hairs of all the panels, or the correct position of the source. 18

2.8 A horizontal array (2.35 km), source ($x = 1.17$ km and $z = 2.39$ km), and velocity model. 19

2.9 Focusing due to a buried horizontal array above the source. 21

2.10 Dense dual array geometry, source (x = 1.17 km and z = 2.39 km), and velocity model. 22

2.11 Focusing due to a dense dual array (23 receivers in each monitor well) located on two sides of the source ($x = 1.17$ km and $z = 2.39$ km). 23

2.12 Sparse (9 receivers in each monitor well) dual array geometry and velocity model. 24

2.13 Focusing due to a full-aperture array (a) and a sparse dual array (b) surrounding the source. 25

2.14 Short, dense dual array geometry and velocity model. 26

2.15 Focusing due to a short dense dual array surrounding the source. 27

2.16 Similar to the synthetic example, focusing due to a short, dense dual array using field data. 29

2.17 Short, dense single array geometry and velocity model. 30

2.18 Focusing due to a short dense single array above the source. 31

2.19 Focusing due to a short dense single array above the source and target formation using field data. 33

3.1 An incorrect source onset time does not allow the wavefield to focus at the correct position in space or time. 38

3.2 Time of focusing at the source location in space with respect to time, when the source onset time is non-zero. 39

3.3 Cross-correlation between the observed (incorrect onset time) and calculated (correct onset time) wavefields at the source position in space. 40

3.4 Cross-correlation between the observed (incorrect onset time) and calculated (correct onset time) wavefields tacked over space. 42

3.5 Synthetic example: Time of focusing at the source location in space and time, occurring at a non-time zero. 43

3.6 Focusing in space and time at the source location, corrected so that the source onset time is at time zero. 44

3.7 An incorrect source onset time does not allow the wavefield to focus at the correct position in space or time. 46

3.8 Synthetic example: Time of focusing at the source location in space and time, occurring at a non-time zero. 47

3.9 Cross-correlation between the observed (field) and calculated (synthetic) wavefields at the source position in space. 48

3.10 Cross-correlation between the observed (field) and calculated (synthetic) wavefields at the source position in space. 49

3.11 Synthetic example: Time of focusing at the source location in space and time occurs at a non-time zero. 50

3.12 Focusing in space and time at the source location, with corrected time so that the source onset time is at time zero. 51

4.1 True velocity model. 55

4.2 Focus obtained using a smoothed, zero-mean velocity model given a short, dual array. The velocity values are the same as seen in Figure 2.3. 56

4.3 Focus obtained using a fast velocity model given the case study geometry shown in Figure 4.1. 58

4.4 Focus obtained using a slow velocity model given the case study geometry shown in Figure 4.1. 59

4.5 A comparison between (a)calculated data d^{cal}, (b) observed data d^{obs}, and (c) the data residual d^{res}. The events in d^{cal} arrive at a time greater than one-wavelength difference from the events in d^{obs}, causing cycle-skipping in d^{res}. 63

4.6 Objective function $J(m)$ that minimizes the data residual d^{res} with respect to % scaled slowness anomaly. 65

4.7 The (a) calculated wavefield focus, (b) ideal focus, and (c) image residual. . 67

4.8 Objective function that minimizes wavefield inconsistencies in the image due to an imperfect velocity model. 69

B.1 Vp well log (black), Backus Averaged Vp (blue) The vertical axis is depth in km and the horizontal axis is velocity in km/s. 85

ACKNOWLEDGMENTS

This masters thesis could not have been completed without the dedicated support and help from my committee members, colleagues, research teammates, friends, and family. Thank you to my committee members, Prof. Paul Sava, Prof. Mike Batzle, Prof Terry Young, and Dr. Jason Gumble for all of your patience, technical advice, and constant push and challenge during my time at Mines.

Prof. Paul Sava, my *lovely assistant* during the CSM Geophysics field session, presented a constant challenge to explore and read as much as I could regarding microseismic. He challenged me everyday to go beyond my comfort zone academically and excel at everything I try. My *real advisor*, Iulia Sava, was especially helpful when it came to letting-go and having a wonderful laugh now-and-then. Thank you, both!

Prof. Mike Batzle, you have given me so many wonderful experiences here at Mines. Thank you for allowing me the opportunity to practice *dance your thesis* during the reservoir development class, and teaching me that we don't care about the rocks themselves, rather we care about *what's in 'em.* It was a pleasure to work with you throughout the past few years during field session, too!

Prof. Terry Young, you showed me how to take on life's challenges head first, and when life was the most stressful, you and Nadine Young encouraged me to play hooky and swing that golf club in order to relax a little and enjoy the beauty life has to offer! Golfing and your classes have been a wonderful experience. I cannot thank you enough for all that you have taught me and done for me throughout my time at Mines!

Dr. Jason Gumble, thank you for all that you taught me during my internships with Cimarex Energy. It was an absolute pleasure working with you last summer as a team to explore the difficult problems associated with microseismic imaging and modeling. You

have been a tremendous help working on and writing my thesis. I really look forward to being your colleague soon!

John Lambuth, thank you for making it possible to use Cimarex's microseismic data for my thesis project. Your data helped validate my work done with synthetic modeling. Thank you for providing the much appreciated technical expertise surrounding the subject of microseismic monitoring, processing, and interpretation. I am very excited to work with you at Cimarex Energy when I start full time.

Mom and Dad, when I was in high school you'd sit down with me and make me stay up late at night until I finished my papers, studied enough for exams, and compelted my homework. I hated all of the grammer and words you'd make me learn and I certenly dispised the fishsticks we'd eat when a grade came back less-than-satisfactory. Now, I appresiate the value of what you have done for me and I cannot thank you enough. All of those late nights wroking on grammer and word choice, certenly, gave me the discapline and knowledge to write this manuscirpt. Thank you!

Diane Witters, you need a special thanks, too, because of all of your help with technical writing! You have picked up where my parents ended with writing. You gave me a new tool to add to my writing tool belt. You have also provided many wonderful smiles and discussions on how to be more involved at Mines. Thank you!

Ricky Yaner, my best friend, thank you for putting up with all of those times I quit writing out of frustration and confusion and became slightly whiney because of those *difficult* classes. You encouraged me to stick with my MS program and give it my best try. Thank you so much for being my shoulder to cry on and my best friend who gave me a wonderful escape away from the hard work at school. Thank you, also, to your wonderful family for supporting me throughout this process.

Dawn Umpleby, thank you for being my Geophysics Mom! You kept me sane the past five-ish years here. You gave me so many, and very much needed, laughs and smiles! After a long day of work, you'd always have that magical power to bring a happy smile to

everyone's faces! Thank you!

I-Team, my research team at CWP, has been my backbone throughout my endeavor to finish my MS degree. You were always there for technical and moral support and provided some of the best advice and technical help. Thank you Jeff, Esteban, Tony, Tom, Francesco, and Natalya! Thank you, also, to my CWP colleagues for all of the long discussions about coding, migration theory, inversion, and life in general. It was a pleasure to work with all of you!

The folks of CGEM, there are no words that can describe how electrifying you are! The dancing, cake, lunch dates, and many many jokes have been so wonderful! My time here with you can never be reversed. The Mines inversion has reached a point of convergence, with all the criteria soon to be met. I regret, it is now time to move-out and begin a new life chapter. Even though sometimes the jokes weighed me down, the overall experience was a positive anomaly! Your technical help and overall friendship have helped me tremendously through my adventure at Mines.

GP Department, my friends, thank you for the many BBQs, help sessions, bowling excursions, life lessons, thesis advice, and memories never to be forgotten. Without you, I would not be who I am today.

Chapter 1

INTRODUCTION

With the advent of hydraulic fracturing, unconventional gas plays are completed and produced more than ever. Given that hydraulic fracturing is an essential technology for oil and gas reservoir completions, operators need to monitor the behavior and extent of the stimulated fracture networks. The high pressure pumping of fluids into the target formation causes a significant increase in pressure in and along the wellbore. When the pressure reaches a failure threshold, preexisting fracture networks reactivate. The failure of the rocks, or reactivation of fracture networks acts as a seismic source. Microseismic monitoring arrays then detect the seismic signatures of the rock failure. Given the link between rock failure and microseismicity, monitoring ideally gives us the opportunity to image the depth, location, geometry, extent, and growth patterns of the fractures (Hubbert, 1957). Often, the interpreters and engineers use the microseismically active volume as a direct indicator of the stimulated reservoir volume under the assumption that microseismic event hypocenters correlate to the orientation, height, length, and density of the stimulated fracture network (Hayles *et al.* , 2011). Microseismicity is a widely used indicator of fracturing in a reservoir due to hydraulic stimulation.

Operators need the ability to map where the rock is breaking so that they can make management decisions about current and future stimulation procedures and can effectively and accurately model the predicted reservoir reserves. With fractures characterized through microseismic monitoring, one may incorporate microseismic maps into hydraulic fracture design and reservoir models. This routine, however, requires a level of consistency and repeatability among microseismic monitoring and processing that is not yet demonstrated

by current practice (Hayles *et al.* , 2011). To be able to locate microseismic events with accuracy and high resolution, I demonstrate in this thesis that we need sufficient acquisition aperture, a known source onset-time, and an accurate velocity model. If one of these three components is missing, we cannot accurately identify and position microseismic events. Throughout this thesis, I use synthetic and field data to address each of these imaging requirements and to study the effect each has on the ability to image microseismic events.

There are two primary methods of acquiring microseismic data. One technique places a sensitive receiver array in an offset well at a depth close to the reservoir to be stimulated. Common practice uses a limited acquisition aperture typically placed in only a single monitor well. This, as I show in Chapter Two, gives rise to event identification limitations during processing. Due to the limited aperture, it is difficult to constrain the location and horizontal and vertical extent of the microseismic event. Multiple monitor arrays reduce the location uncertainty, but the array aperture may still not be sufficient to resolve the exact location and size of the microseismic event temporally and spatially. In Chapter Two I present theoretical and field geometries ranging from a full-aperture to realistic geometries with the aim of quantifying the effects of varying degrees of array aperture on the ability to locate a microseismic event.

Typically, only a single well is available to monitor a hydraulic fracturing job. Incorporating multiple monitor wells is a function of availability and economics, making multiple monitor arrays an exception. One often uses old reworked wells to monitor microseismic events. Drilling a well simply for monitoring purposes is costly, giving little flexibility of monitor array positioning. Incorporating multiple monitor wells provides significant advantages in processing, however, and needs to be considered when designing a microseismic monitoring survey. Incorporating multiple monitor arrays in the microseismic survey helps to constrain the spatial and temporal extent of the microseismic events (Abel, 2011; Grechka, 2010; et. al., 2010b).

If boreholes are not available to monitor hydraulic fracturing, another viable method

of microseismic acquisition consists of a two-dimensional surface array spreading the extent of the stimulated area. Microseismic events are much easier to constrain horizontally using a surface array. The surface array, however, fails in the ability to constrain microseismic events vertically, as there is little information to constrain the depths of the microseismic events. In addition, the signal to noise ratio is much lower given a surface array. Naturally, the array is much farther from the source and is subject to noisy rig operations on the surface (Maxwell & Urbancic, 2001; Zimmer, 2012).

The distance of the monitor array from the zone being stimulated affects the ability to detect events in the monitoring array, regardless of array geometry (et. al., 2010b). Due to attenuation, dispersion, and geometric spreading, the microseismic data are degraded, perhaps even undetectable, given the distance between the source and receivers and the area's velocity profile (Zimmer, 2012; Warpinski et. al., 2005). Even with optimum array placement and positioning, microseismic data may be overwhelmed by noise. Common sources of noise include pad operations, drilling noise, and production. Wellbore vibrations, machinery, and seismic surveys are also present. Fluid flow, wind, and other natural sources of noise may deteriorate or mask the microseismic signal and should be mitigated as much as possible (Maxwell & Urbancic, 2001). One method used to mitigate noise, for example, is to burry the surface array geophones. Besides noise, deviation surveys of the stimulation and monitor well(s) and/or surface array must be accurate, as the affect the quality and accuracy of microseismic monitoring. Accurate surveying of the locations of sources and receivers is a necessity; otherwise, inaccurate surveys lead to errors in positioning of microseisms.

Once contractors collect the data, processing is done either by using P- and S-arrival picking coupled with hodogram analysis, ray-tracing theory, and a grid search for the best fit microseismic event location (Warpinski et. al., 2005), or by using reverse time imaging, which exploits the entire acquired wavefield (Artman, 2010; Xuan, 2010).

A grid search is the most common processing practice. Assuming the velocity structure is correct, we use ray-tracing to evaluate P- and S-wave arrival times. We then partition

the velocity model into grid points, where arrival times and polarizations are calculated for every point in the grid (given a particular array geometry). One then compares these forward modeled arrival times and polarizations to the picked P- and S-arrival times and polarizations from the field data, assuming that the point in the Earth where the field data best fits the forward modeled times is the best fit location of the microseismic event (Warpinski et. al., 2005; Rentsch, 2007).

Local Earthquake Tomography (LET) takes the location algorithm a step further and utilizes the difference between the observed and calculated time to simultaneously find the best fit hypocenter location and update the velocity model (Thurber, 1992). Without velocity model calibration, hypocenter locations are inaccurate and defocused. To update a velocity model, the starting model must be as close to the true model as possible. An investigation of LET (Appendix A) shows that it is a viable technique in microseismic processing, but may fail if data are corrupted by large noise levels.

Reverse time imaging is a less utilized technique for locating microseismic events, but a technique more robust in the presence of noise. To overcome the difficulties associated with picking P- and S-arrivals, automatic techniques based on reverse time imaging eliminate the need for arrival identification. Reverse time imaging is capable, in principle, of focusing microseismic energy at its source position and at its trigger time, even when data are corrupted by high levels of noise (Artman, 2010; et. al., 2011; Xuan, 2010). In Chapter Two, I explore the benefits and pitfalls associated with reverse time imaging and emphasize the need for wide aperture in microseismic acquisition.

The application of reverse time imaging requires the knowledge of the source onset-time. To directly measure the onset-time of the source, one may deploy a specific tool which measures current fluctuations caused by the perforation shot detonator. Using these current fluctuations, one may deduce the onset-time of the perforation shot (Uhl, 2006; Warpinski et. al., 2005) with high degree of accuracy. However, the source-onset time is not always available. Without the knowledge of the onset-time of the source it is difficult to update a

velocity model. Similarly, without an accurate velocity model one cannot accurately locate a source. Without any given source onset-time, we are left with a severely underdetermined problem, a problem that is inherently non-unique. To overcome this impasse between the unknown source onset-time and an imperfect velocity model we must make an assumption about the velocity: The model used to propagate the wavefield has the same mean as the true velocity model. Making this assumption, we may inspect the wavefield and determine the correct shift needed so that the source occurs at the correct onset-time. In Chapter Three, I discuss a technique using wavefield focusing to estimate source onset-time if direct timing measurements are unavailable.

LET naturally works for updating velocity models when one uses ray tracing to locate hypocenters. Similarly, we could use waveform tomography to update a velocity model when we use reverse time imaging to locate hypocenters. Rather than minimizing the travel-time residuals like in LET, it is possible to incorporate the full waveform (i.e., phase, frequency, and amplitude) in the process of updating the velocity model (Virieux, 2009) by both inspecting the observed and calculated wavefields at the receiver positions and at the source positions. Investigating the wavefield in this manner is referred to as data and image domain, respectively. Using the full waveform introduces complications when applied to the microseismic case in the data domain. We use the full waveform of the microseismic source to calculate a residual between the observed and calculated data. In the data domain, this implies that the source function must be known and must be of low frequency as to not induce cycle skipping (Virieux, 2009). We often do not know the microseismic source functions, even perforation shot functions. In addition, these source functions often contain high frequencies, on the order of kHz. The combination of the unknown source function and the high frequency nature of microseismic sources shows that data domain waveform tomography is impractical to apply to microseismic. image domain tomography, on the other hand, eliminates the issues present in data domain tomography (Yang, 2011). However, the final velocity model obtained through image domain tomography cannot achieve the same

resolution as that seen in the data domain. In Chapter Four, I present both the data and image domain tomography methods along with the objective functions for each.

Regardless of the method implemented to refine the model, incorrect velocity leads to spatial and temporal smearing and misplacement of the microseismic events. In Chapter Four I present different methods for updating a velocity model and I also explore the effects of propagating a microseismic wavefield in an incorrect velocity model.

Chapter 2

APERTURE EFFECTS ON WAVEFIELD FOCUSING

Reverse time imaging is a valuable tool for locating microseimic events. Wavefield focusing which indicates microseismic locations in space and time is a function of receiver array aperture. Present day monitoring techniques have limited aperture, negatively impacting the wavefield focus around the source location. A smeared focus results in large uncertainties in source location and timing.

Using a sequence of different array geometries ranging from a full-aperture array to the widely used limited aperture borehole array, I estimate the applicability of current industry monitoring techniques and advocate for the use of wide-aperture arrays. In this thesis, I show the wavefield focusing for each receiver array geometry and compare it to the focusing obtained using an ideal full-aperture array. Results show that current monitoring techniques do not incorporate enough aperture needed to image sources accurately.

2.1 Introduction

Aperture is a significant challenge facing the microseismic community and is defined as a window that limits the amount of information recorded; it is the size and positioning of a survey needed to accurately image an area of interest. In surface seismic, the aperture needed to accurately and precisely image a target is a function of formation velocities, geologic structure and dip, culture (e.g., buildings, protected wildlife areas, etc.), and economics. A larger receiver array provides more information for increasing the resolution, accuracy, and precision of an image.

Before delving into the effects of aperture, I need to develop a basic understanding of

the techniques used to locate microseismic events by acoustic reverse time imaging. This method presents significant advantages over conventional microseismic event location techniques because it succeeds where conventional techniques fail. Conventional methodology relies on picking first break P- and S-arrivals and propagating this information using ray tracing (Warpinski et. al., 2005; Rentsch, 2007). If high levels of noise are present in the data, picking first-break arrival times is a difficult task producing large residuals between the forward modeled and observed data, respectively (Bose *et al.* , 2009). Large residuals result in a higher event hypocenter location uncertainty. Reverse time imaging eliminates the need for arrival picking, avoids the use of the grid search method, and addresses the issues of noise(Artman, 2010). I illustrate with field and synthetic examples later in this chapter the robustness of reverse time imaging in the presence of noise.

To locate an event, reverse time imaging relies on investigating the degree of wavefield focusing around the event location near the vicinity of the onset time of the source. This method is particularly useful for locating events when the source onset time is unknown; we can manipulate the wavefield forwards and backwards in time and assess the degree of wavefield focusing with respect to time. If the velocity model and timing measurements are correct, we observe the focus at time-zero. Accordingly, we are accustomed to having the image defined as the focusing of the wavefield at time-zero. My data are not perfect and do not include any measurement of the source onset time. Because of this, I change the definition of what an image is, slightly, by incorporating a small time window around time-zero. Henceforth, whenever I refer to an *image*, I am describing the wavefield in a small time window around the onset time and source position. According to my definition, an image has three dimensions in 2D (x, z, and t) or four dimensions in 3D (x, y, z, and t). I represent the images using three intersecting slices, as shown in Figure 2.1.

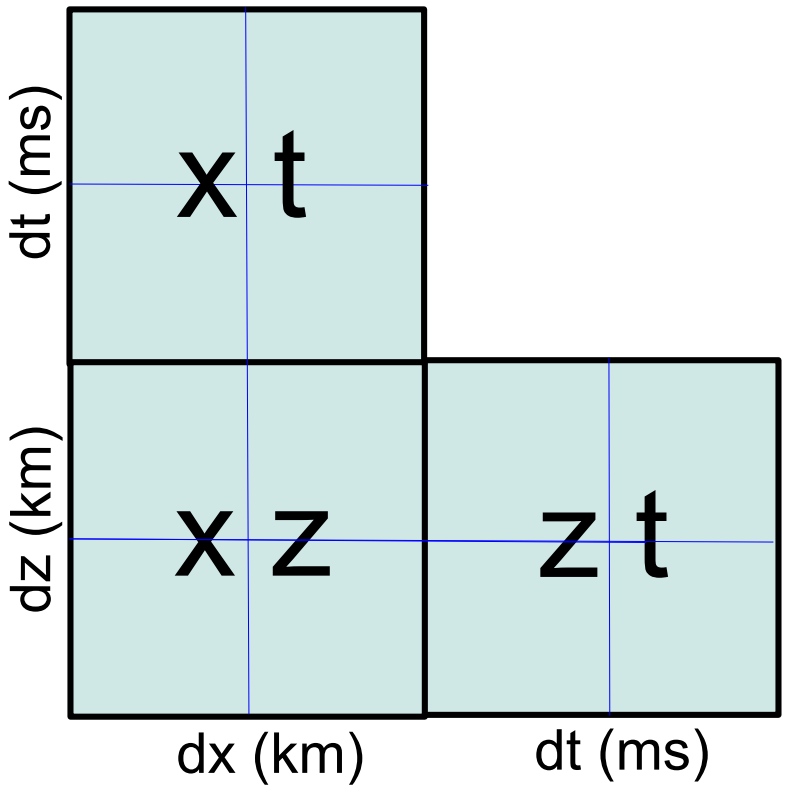


Figure 2.1. A simple cartoon illustrating a three-dimensional slice in the wavefield around the source location (e.g., A perforation shot in the examples to follow). The top left panel is the $x-t$ plane of the wavefield in space and time, the bottom left panel is the $x-z$ plane in space, and the bottom right panel is the $z-t$ plane in space and time. The axes of the panels are the change in space and time with respect to the absolute position of the source location. The change in space and time is measured in km and ms, respectively.

The top left panel is the $x-t$ domain, illustrating how the wavefield propagates through time with respect to x, given a fixed z position. Similarly, the bottom right panel is the $z-t$ domain which illustrates how the wavefield propagates through time with respect to the z-domain given a fixed x-coordinate. The center panel is the $x-z$ domain and shows the wavefield focus given a set point in time. The crosshairs in each panel of Figure 2.1 denote the absolute location of the source in space and time.

In a constant homogenous medium, we expect the wavefield to propagate evenly in all directions with respect to time, creating a spherical wavefront. In two-dimensions, the wavefront appears to propagate as a circular fashion with respect forward-marching time. If we eliminate a spatial variable by inspecting the wavefield propagation at a fixed point in space (e.g. $x = x_{sou}$ or $z = z_{sou}$), the wavefield propagates away from this source evenly in space. When we reverse the time-axis of the wavefield so that it propagates beyond the source onset time, the wavefield defocuses and, again, propagates away from the source in x and z. We refer to forward and reverse time as positive and negative time, respectively. In both negative and positive time, the wavefield appears as two cones, one convex and one concave, with the apex of both cones located at the source origin in the $x-t$ and $z-t$ domains. In a heterogeneous model, as is the case with my field case study, the cone pattern is not perfect but is still recognizable. At the correct source onset time, in both homogenous and heterogeneous models, we expect to see a perfect focus in the $x-z$ domain. If we capture wavefield information from all directions, and assume that the velocity model and timing information is correct, the wavefield focuses to a point in x, z, and t at the correct location of the source in space and time. Note that any deviation from the true location of the source, or the intersection of the crosshairs in the panels, indicates an imperfect focusing in the wavefield due to source frequencies, aperture affects, incorrect timing, and/or velocity errors. I discuss each factor affecting the degree of focusing in the remaining chapters of this thesis.

The source frequency used in all of the synthetic modeling is 150 Hz. Microseismic

frequencies range much higher than this, but I choose a source frequency of 150 Hz for the purpose of computational and cost and stability. Higher frequencies cause numerical instabilities in the modeling, with a computation cost that increases proportionally with frequency. A source of 150 Hz does not cost much computationally and still lies within the natural microseismic frequency range allowing for a higher resolution image. The resolution limit of the velocity model, however, is determined by the source frequency. Given that the minimum and maximum velocity values used for forward modeling are 4.63 km/s and 5.86 km/s (discussed in detail later in this chapter), respectively, we calculate the expected resolution using principles borrowed from diffraction theory. The expected resolution limit of a diffraction focus is half the of the source wavelength. Accordingly, we expect that the best possible image resolution lies between ± 15 m and ± 20 m. We may only obtain this maximum resolution if the velocity model and source onset time are correct and if we capture wavefield information from all directions (i.e. large acquisition aperture).

In surface seismic, *wide* aperture is commonplace and highly desired. Large apertures are not common in microseismic monitoring. Often, industry deploys small surface arrays and short and dense downhole arrays, which drastically limit the microseismic acquisition aperture, and thus, the ability to accurately and precisely locate events (Eisner, 2010; Grechka, 2010). The question then arises as to how these aperture limitations affect the ability to focus the microseismic wavefield. Figure 2.2 shows the effects of aperture on the ability to focus the wavefield. The bottom panel in Figure 2.2 shows the ideal focused wavefield (near the cross-hairs in the panels). The top panel in Figure 2.2 shows the same wavefield focusing if the aperture is less-than-ideal. Missing wavefield information inhibits our ability to focus the wavefield to a point in space and time. Without full-aperture, there is a certain degree of ambiguity in the wavefield, resulting in a wavefield focus which is smeared in both x and z with respect to time. Smearing simply means that the wavefield does not focus to the highest-resolution point possible. Smearing includes but is not limited to defocusing, side-lobes, and distortion of the focus.

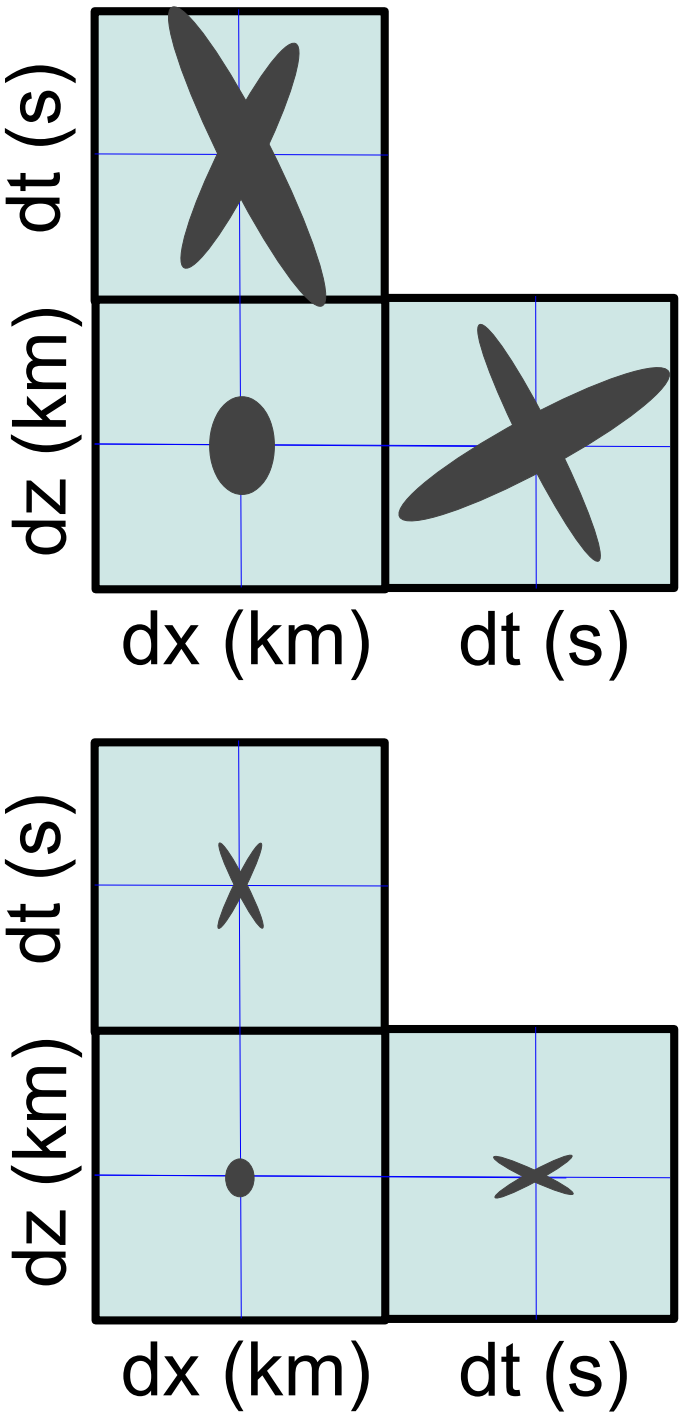


Figure 2.2. A poor aperture (top) defocuses the microseismic event, whereas a full-aperture (bottom) provides the best resolution of the focus.

When the velocity model and source onset time are correct and we capture wavefield information from all directions, the wavefield focuses to a point, as seen in the bottom panel of Figure 2.2. However, when wavefield information is missing, the wavefield does not focus to a point, causing smearing in the focus seen in the top panel of Figure 2.2. The less wavefield information we record, the less the wavefield focuses to a point.

To illustrate the need for wide acquisition aperture in microseismic monitoring, I present a synthetic example which includes two vertical monitor wells and a horizontal well which was perforated and stimulated using hydraulic fracturing. The two vertical wells contain geophone arrays of 11 receivers, with a 15.24 m spacing (50 ft). The stimulation well contains five stages with four perforations shots per stage, amounting to 20 perforation shots total. A stage is a segment of the stimulation well containing a certain number of perforation shots which is isolated at any given time during the hydraulic fracturing process. Figure 2.3 shows the source-array geometry as well as the velocity used in forward modeling. The velocity values range from from 4.63 km/s (19, 200 ft/s) in dark grey to 5.86 km/s (15, 200 ft/s) in white.

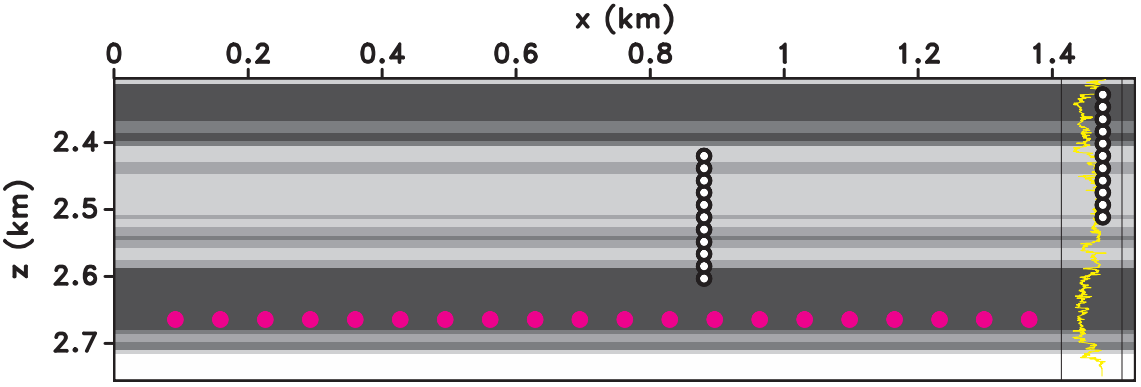


Figure 2.3. Case study: dual borehole array (receivers located in the monitor wells at $x = 0.88$ km and $x = 1.47$ km), 20 perforation shots (located at $z = 2.67$ km), and the sonic velocity log used to produce the 2D velocity model (overlaid on right). Velocity values range from 4.63 km/s in dark grey to 5.86 km/s in white.

I construct an initial velocity model, shown in Figure 2.3 from a sonic log, upscaled from sonic frequencies to seismic frequencies using Backus Averaging (Appendix B). I extend this upscaled, one-dimensional velocity model into two-dimensions in order to generate a model usable given the near-two-dimensional acquisition geometry. I assume the model to be acoustic and the density to be constant. This assumption implies that we cannot model elastic properties such as S-wave arrivals and anisotropic parameters.

The velocity in the initial model ranges from 4.63 km/s (19,200 ft/s) to 5.86 km/s (15,200 ft/s). Upon initial inspection, I questioned the validity of the velocities values, as they appear to be high. To verify the velocity values, I analyzed the well logs and lithologic information. These velocities correspond to highly cemented sandstones. Figure 2.4 shows a log suite containing a Gamma Ray (GR) log, a Neutron Porosity log converted to a fractional porosity log, a density log, and a compressional velocity log (VP), which support my conclusions that the reservoir is composed of highly cemented sandstones.

In this case study, the reservoir, or hydraulically stimulated zone, is between the depths of 2.6 km and 2.7 km. Initially I suspected that this zone is composed of shales, as suggested by the GR log. Compared to the porosity, density, and VP logs, however, it becomes apparent that the zone of interest is composed of highly cemented sandstone. Note that the density log remains a near constant 2.65 g/cc, the matrix density of quartz. This near constant density seen in the logs justifies my decision to use a constant density model for forward modeling later in this chapter. The porosity is high in relation to the rest of the log, averaging around 15% porosity compared to an average of 5% to 10% in the rest of the log; in the same zone, the velocity is slow, averaging around 4.63 km/s. Typically shales have a lower porosity, higher density, and faster velocity. In this case, the porosity is higher, the density is lower, and the velocity is slower than the rest of the log. Typically shales have a higher GR count, but it is also possible that cemented sandstones have a higher GR as well. All information in the well log suite points towards a highly cemented sandstone.

Once I construct an initial model from the well logs and incorporate the case study

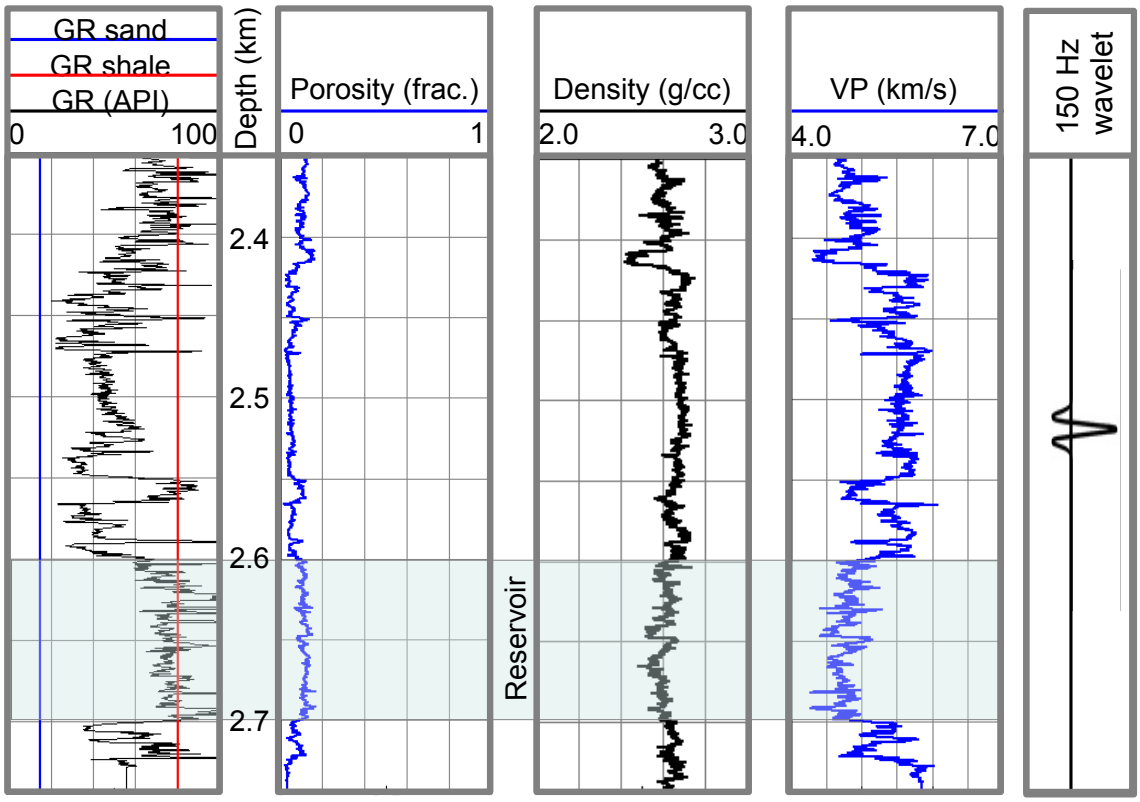


Figure 2.4. Case study: well logs. From left to right: gamma ray (GR), fractional porosity, density, compressional velocity, and 150 Hz wavelet.

geometry, I forward model perforation shots using the two-way wave equation. To reiterate, the density model used to propagate the wavefield is constant and the velocity model is acoustic, meaning that the shear velocity is zero. We then evaluate the forward modeled wavefield at the receiver positions to create synthetic data. Reversing the time axis in both the forward modeled and field data, I inspect the wavefield for places of focusing. Ideally, the events exist where wavefields focus. Therefore, using reverse-time imaging I locate these perforation shot events using synthetic data and compare my results with the same method applied to field data. Both the synthetic and field data are sampled at a rate of 0.5 ms. In this chapter, I focus solely on imaging perforation shots, since the source location in space is known. Figure 2.5 is an example of field perforation shot data used for imaging events.

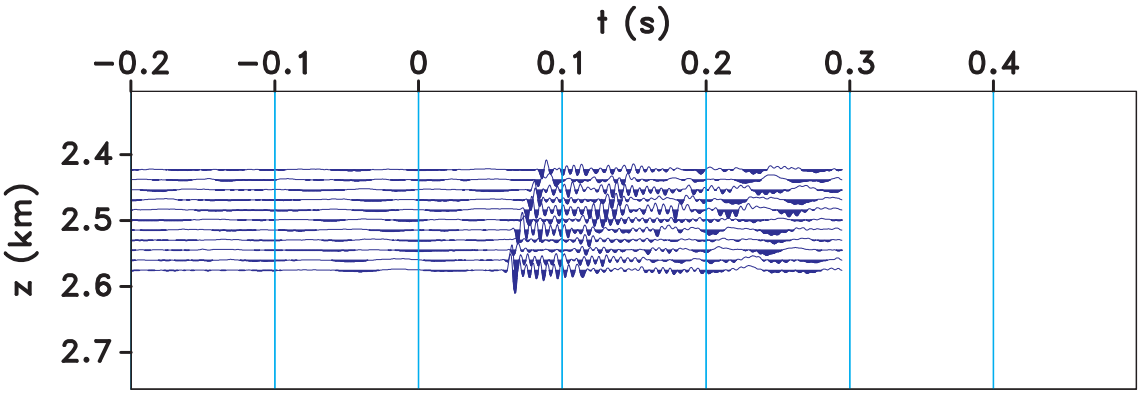


Figure 2.5. Raw, unfiltered perforation shot data used to image the known shot locations. The field data are three-component and elastic in nature. To simplify, I use a single horizontal component of the field data in the simulations and I assume an acoustic medium.

Rather than picking arrivals on the data I pick events where the wavefield focuses. I reverse the observed field data and calculated synthetic data in time and inject these into the receiver locations. The reverse time wavefields propagate through the upscaled velocity model which focuses in space $W(x, z, t = t_{source})$, and in time $W(x = x_{source}, z_{source}, t)$. W is the forward modeled wavefield, x, and z are spatial variables, and t is time.

Presently, we assume that the source onset time is known. If the onset time is unknown, it can severely misposition and defocus the microseismic wavefield and cause errors in event location and uncertainty. We also assume that the velocity which produced the observed and calculated data is the same model used to back-propagate the reverse-time wavefield.

2.2 Effects of Aperture on Focusing

Throughout the investigation of aperture effects, I present several different array geometries, all with the same source position and velocity model, with the purpose of quantifying the effects of aperture on the degree of wavefield focusing. Initially, I show an ideal yet unrealistic *full-aperture* acquisition array and I assess the resulting wavefield focusing around the source location. Next, we explore a surface array, and single and dual downhole arrays of various sizes, receiver densities, and positioning.

2.2.1 Theoretical Array Geometries

In an ideal situation, receivers completely surround the source providing full-aperture coverage seen in Figure 2.6. The full-aperture array captures wavefield information from all directions, allowing us to focus the wavefield to a point shown in Figure 2.7.

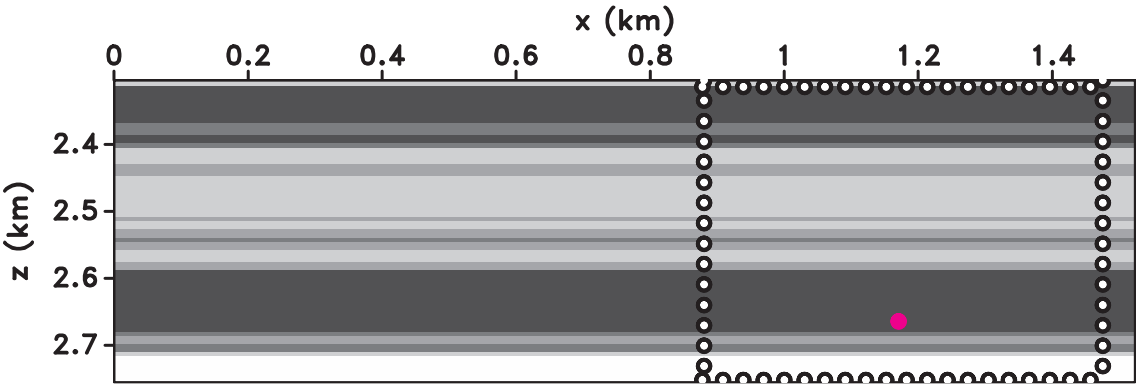


Figure 2.6. Full-aperture array and velocity model. The receiver array (box) is dense and surrounds a single source located at $x = 1.17$ km and $z = 2.38$ km.

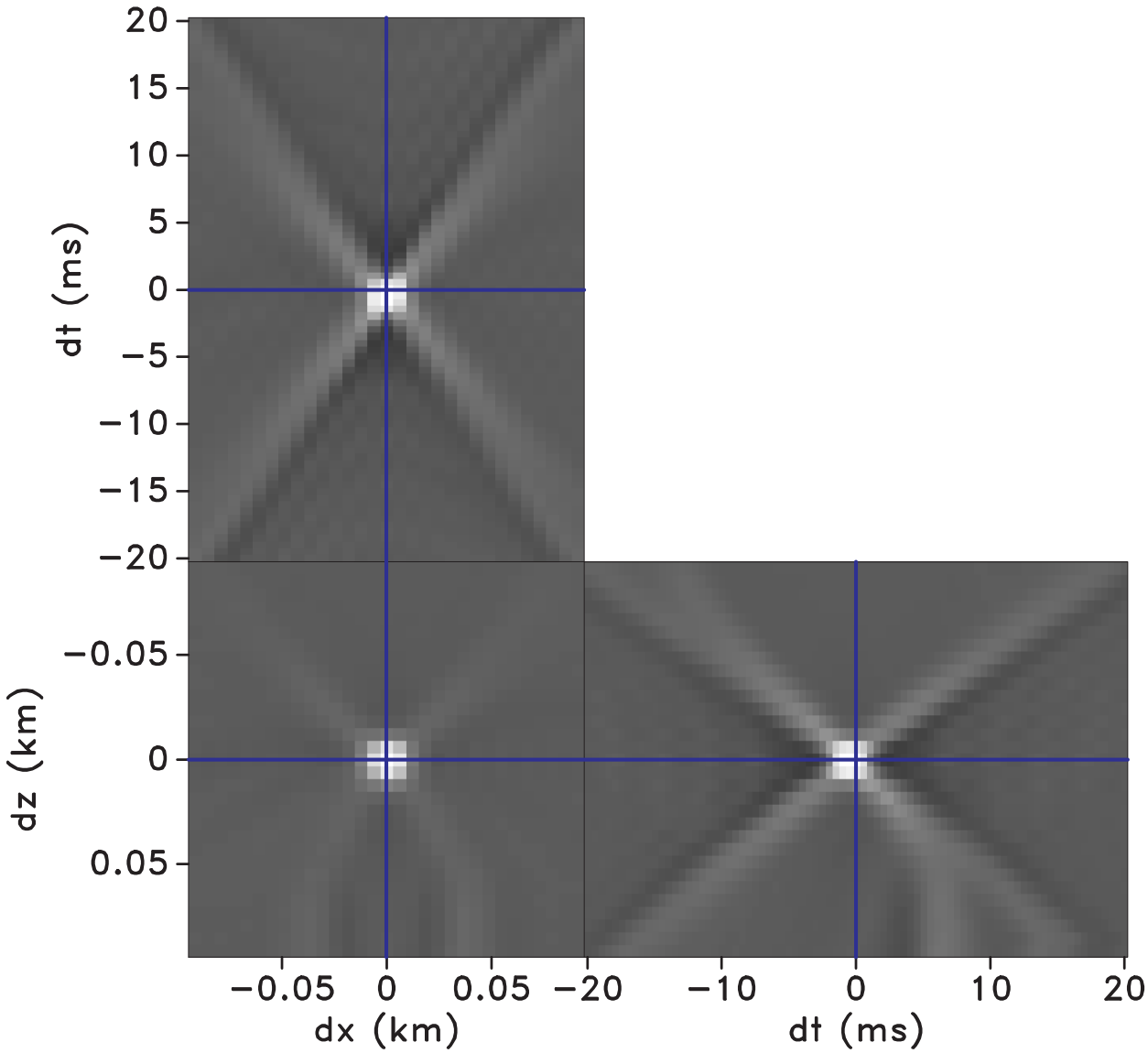


Figure 2.7. Focusing due to a full-aperture box array surrounding the source. The focal point, as expected, resides at the cross-hairs of all the panels, or the correct position of the source.

In reality, such an array is impossible to construct. Figure 2.7 representing a three-dimensional slice in the wavefield at the source location in space and time, illustrates the degree of focusing obtainable. The wavefield appears to have the best focus resolution possible. The resolution of the focal point horizontally and vertically is approximately ± 15 m from the center of the source location in both x and z. This resolution is exactly what we expect, given the source frequency, the full-aperture array, and the true velocity model, described earlier in this chapter. I use this image as a reference for subsequent examples.

A less utilized array geometry is the horizontal array. Sometimes the horizontal array resides on the surface and other times the array is below the surface, either in a wellbore or buried along the surface of the Earth. In the synthetic case shown in Figure 2.8, I model a buried horizontal array which is approximately 2.35 km in the Earth. Note that the velocity model does not begin at the surface of the Earth, rather it too begins at 2.35 km. I model a deeply buried array simply for the purpose of reducing computational costs. As the array gets further from the source, the wavefield focus looses resolution. For example, a surface array has less resolution that a buried horizontal array closer to the source.

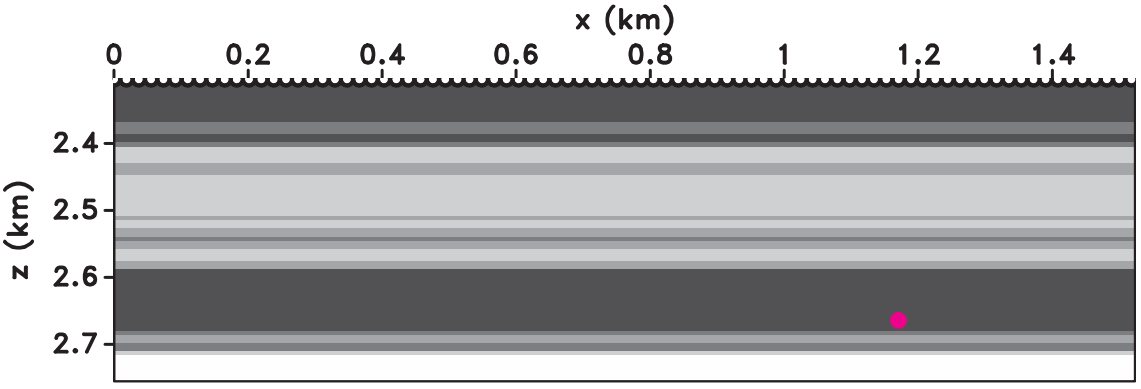


Figure 2.8. A horizontal array (2.35 km), source (x = 1.17 km and z = 2.39 km), and velocity model.

Compared to the focusing achieved from full-aperture array in Figure 2.7, the horizontal array produces vertical smearing of the focus as seen in Figure 2.9. In the $x-t$ plane the wavefield focuses to a resolution similar to that of the full-aperture array in Figure 2.7. In the $z-t$ plane, however, the focusing is poorly resolved with smearing in the $z-t$ plane extending beyond the visible display of the image. The smearing of the wavefield in z implies that if the source onset time is incorrect by ± 20 ms (outside of the visible panel in Figure 2.9), the source can be mislocated by more than ± 100 m (again, beyond the display panel). There is not enough wavefield information to constrain the wavefield in z so that is focuses to a point. For comparison, the reservoir layer is only 100 m. This implies that if the source is located along the edges of the reservoir, the source has the potential to be relocated to a vertical position that lies outside of the reservoir layer. Such misinterpretation results in misguided decisions regarding the future hydraulic fracturing stimulation, well completions, or production procedures (Hayles *et al.* , 2011).

Horizontal arrays are not as common as vertical monitor arrays in industry today. Next, let us explore the effects of theoretical, long dual arrays. Figure 2.10, shows a theoretical, dense dual array geometry that straddles the target formation, containing the source in the center of the array in x. Most vertical monitor arrays typically sit in wells which already exist; they are often temporarily shut-in or even plugged and abandoned. Typically these wells do not extend farther than the target formation, providing little to no information below the formation. If there is a high velocity contrast between the target and the surrounding formations, the source wavefield can be so refracted that much information does not reach the receiver arrays.

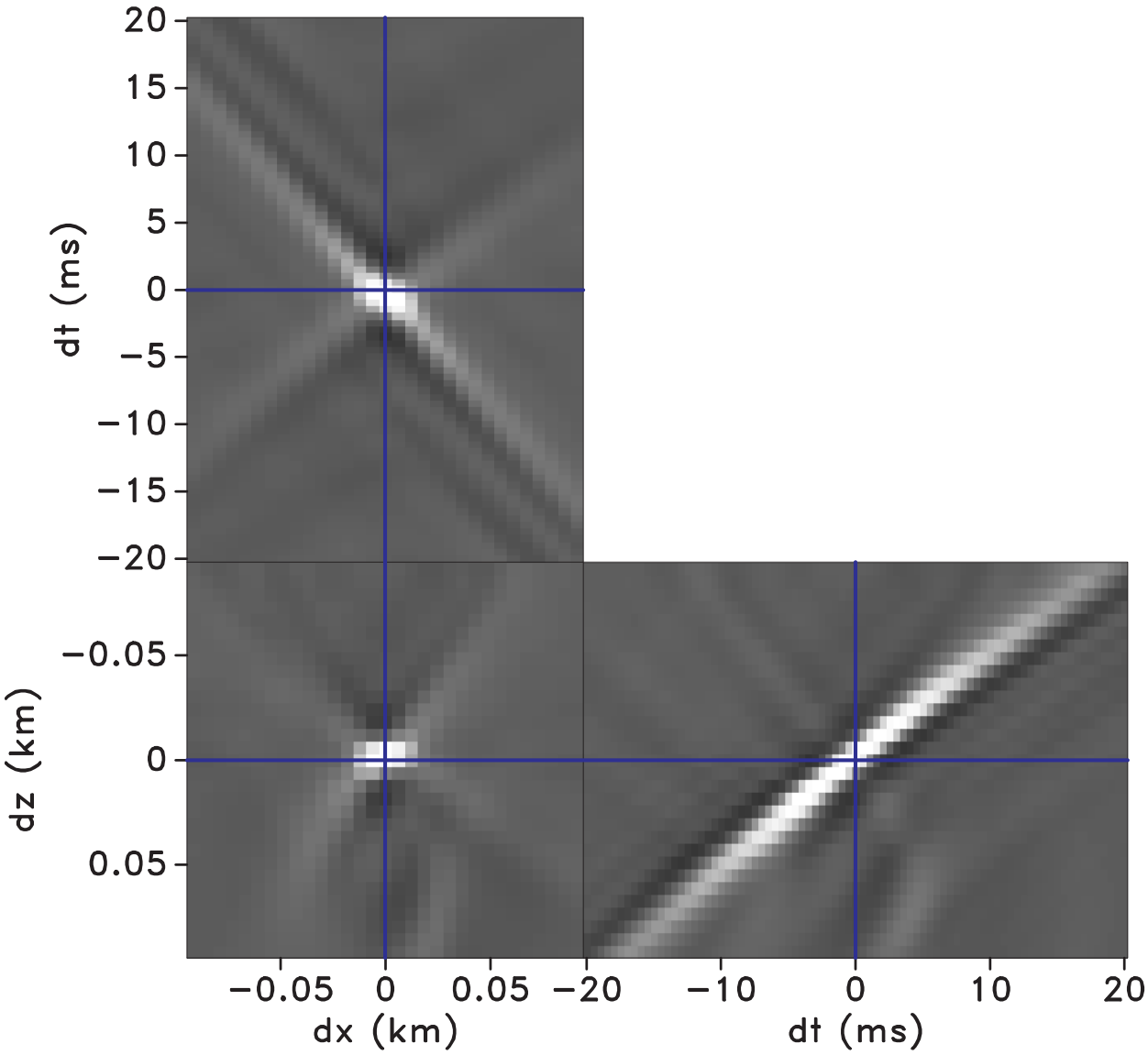


Figure 2.9. Focusing due to a buried horizontal array above the source.

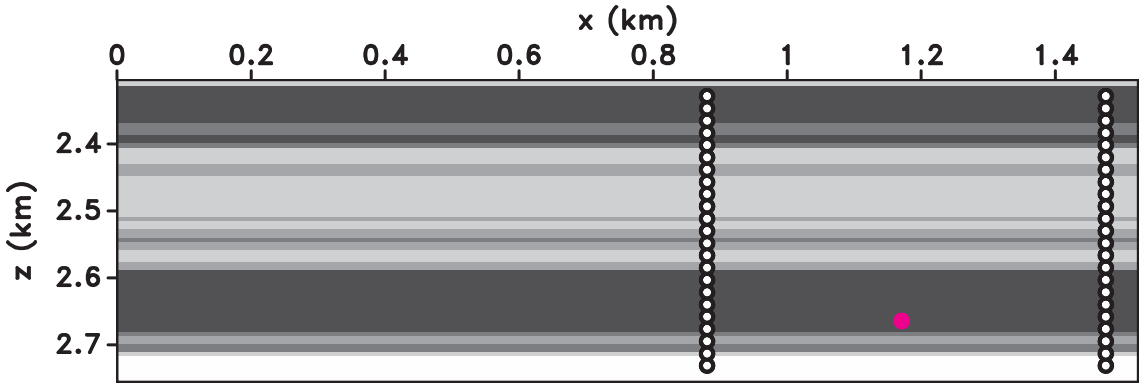


Figure 2.10. Dense dual array geometry, source (x = 1.17 km and z = 2.39 km), and velocity model.

Vertical arrays provide a much better constraint of the wavefield focus if the vertical arrays have a large aperture in addition, they are typically closer to the sources as well as the target formation. Using multiple monitor arrays, there is a better opportunity to record more wavefield information allowing us to focus the wavefield to a point(Abel, 2011; Grechka, 2010; et. al., 2010b). Oppositely, horizontal arrays capture wavefield information from only one direction, not multiple directions as do multiple vertical arrays.

Figure 2.11 shows the focusing attainable from a dual receiver array straddling the target formation with the source in the middle of the wellbores. The dense, dual vertical array in Figure 2.11 produces a wavefield focus that is comparable in resolution with that of the full-aperture array seen in Figure 2.7. There is vertical smearing of the focus in Figure 2.11. Through visual inspection, we observed that in the $x-t$ plane, the wavefield is defocused with an approximate resolution of $\pm$20 m. This is more defocused than what is seen in the ideal full-aperture case in Figure 2.7. The $z-t$ plane shows a focus similar to that of the full-aperture array, lending to an approximate resolution of $\pm$15 m. This is very close to the resolution obtainable using the full-aperture array and the array geometry is much more feasible in reality than an array surrounding the source.

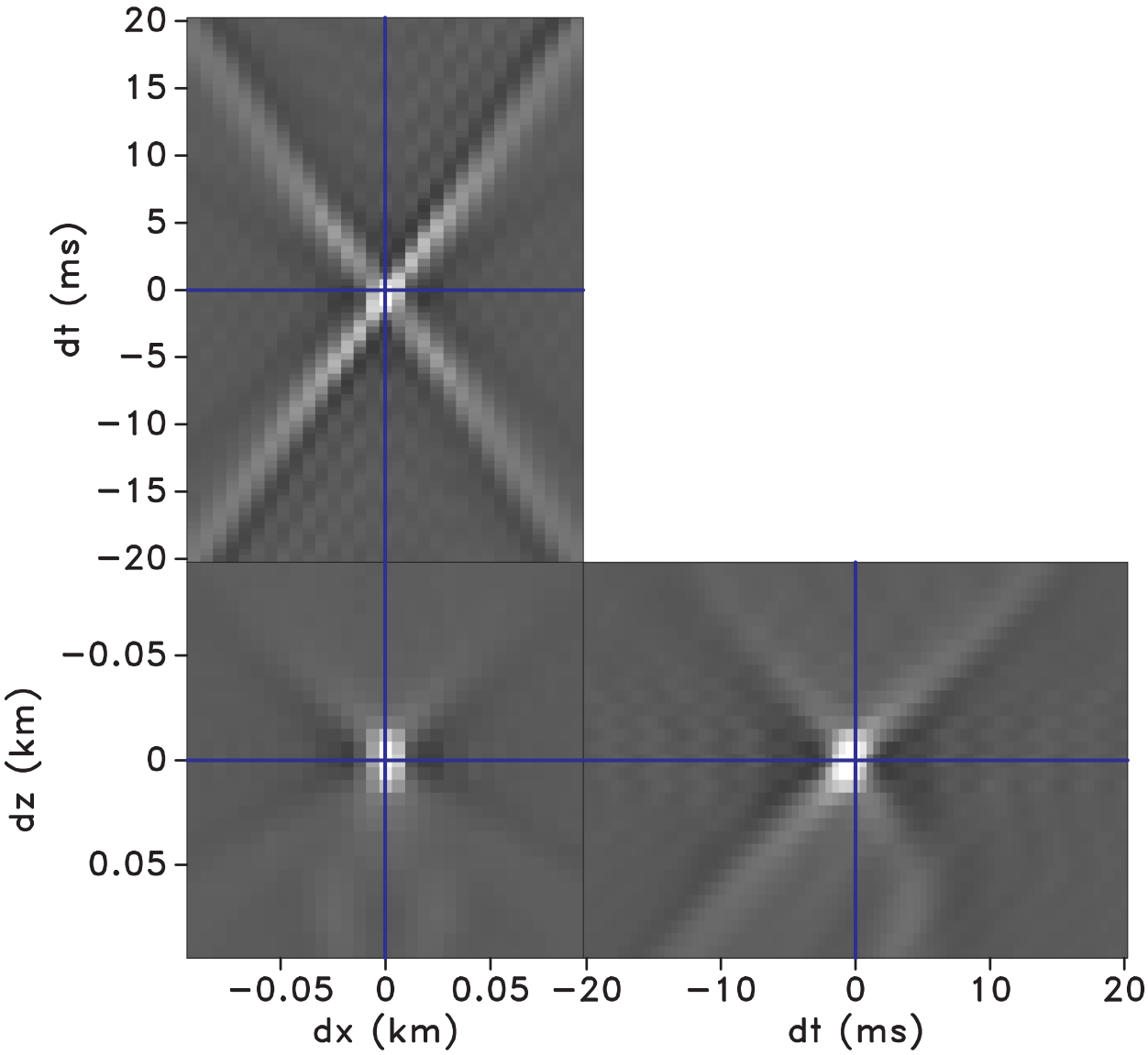


Figure 2.11. Focusing due to a dense dual array (23 receivers in each monitor well) located on two sides of the source ($x = 1.17$ km and $z = 2.39$ km).

Even though this aperture resolves the image nicely, there are realistic limitations preventing the deployment of such an array. Perhaps there is only a certain number of receivers per string with a fixed interval between each receiver. Maybe the cost prohibits the deployment of many geophones. To address these issues, I reduce the number of receivers from 23 in Figure 2.11 to 9 receivers in Figure 2.12.

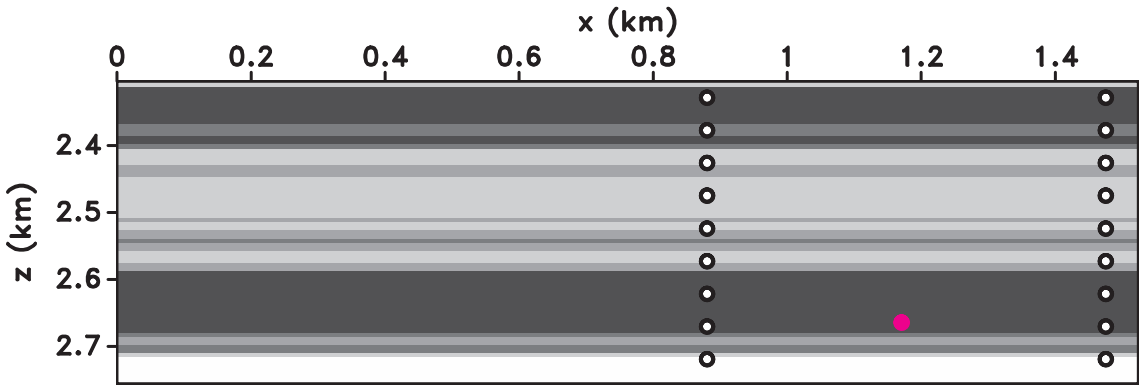


Figure 2.12. Sparse (9 receivers in each monitor well) dual array geometry and velocity model.

The sparser array in Figure 2.12 spans the same vertical distance as the dense array for the purpose of the focusing between the two arrays and evaluating the effect of receiver sparsity. Figure 2.13 illustrates the results. The image in Figure 2.11 is coarser when using the sparser array in Figure 2.13 than when using the dense array. The coarse appearance of the image focus is due to an insufficient sampling in space. Both the $x-t$ plane and $z-t$ plane show a slight defocusing compared to that of the full-aperture in Figure 2.7 and the dense dual array geometry in Figure 2.11. The resolution in x and the z is approximately ± 20 m and ± 20 m from the center of the source location, respectively. This resolution is good compared to that seen in the full-aperture array in Figure 2.7. Cost-wise this is favorable. The amount of receivers decreased and the image quality remained about the same.

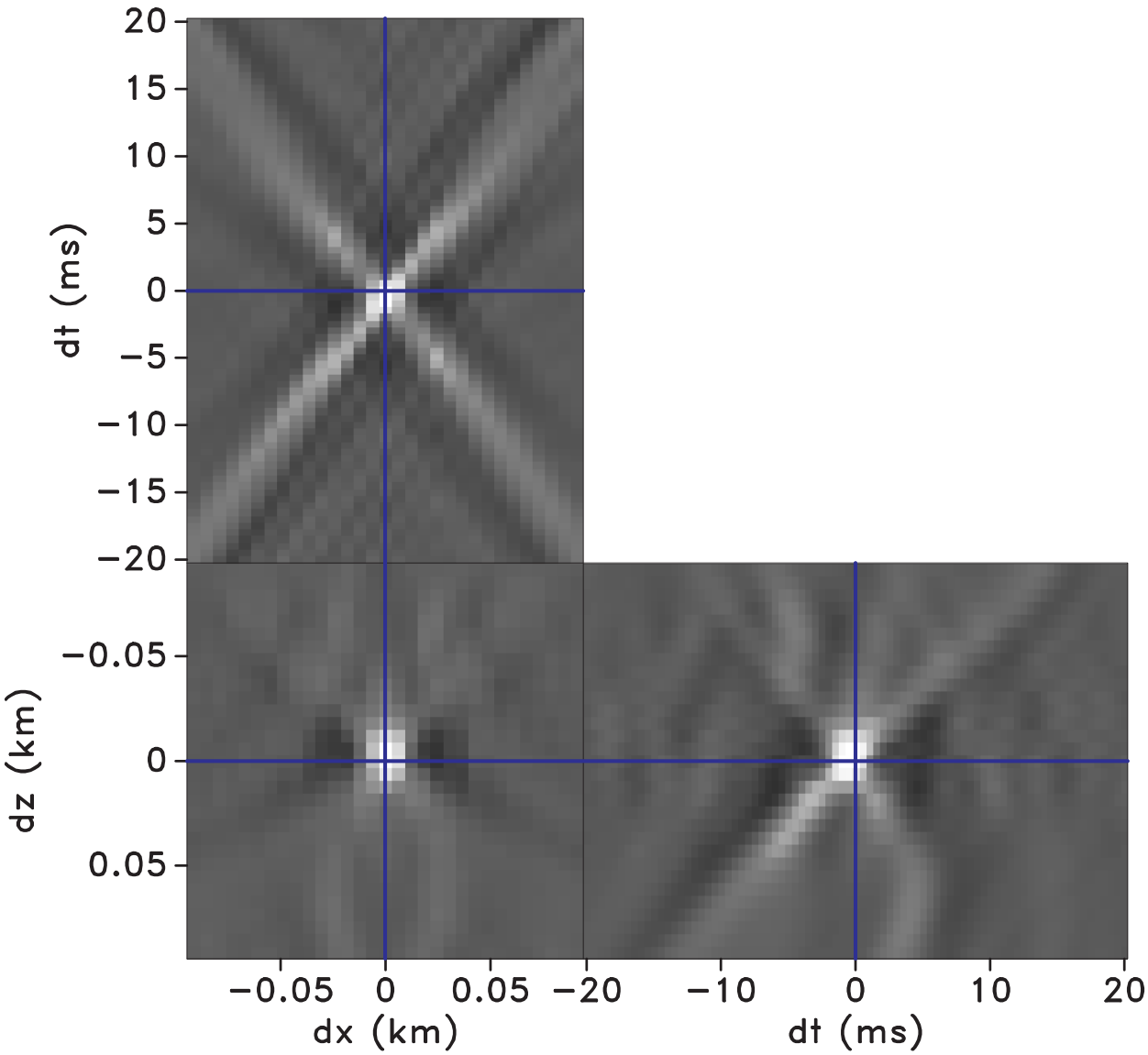


Figure 2.13. Focusing due to a full-aperture array (a) and a sparse dual array (b) surrounding the source.

2.2.2 Case Study Array Geometries

In the previous section, we explored the focusing achievable from four theoretical array geometries with both horizontal and vertical configurations. Applying the information about resolution of focusing learned from these four geometries, one may now examine the focusing achievable from the field case study geometries. The focusing from the short and dense arrays appears to be poorly resolved with vertical and horizontal uncertainties. To begin, I explore the case study array geometry containing two short, vertical arrays, seen in Figure 2.14.

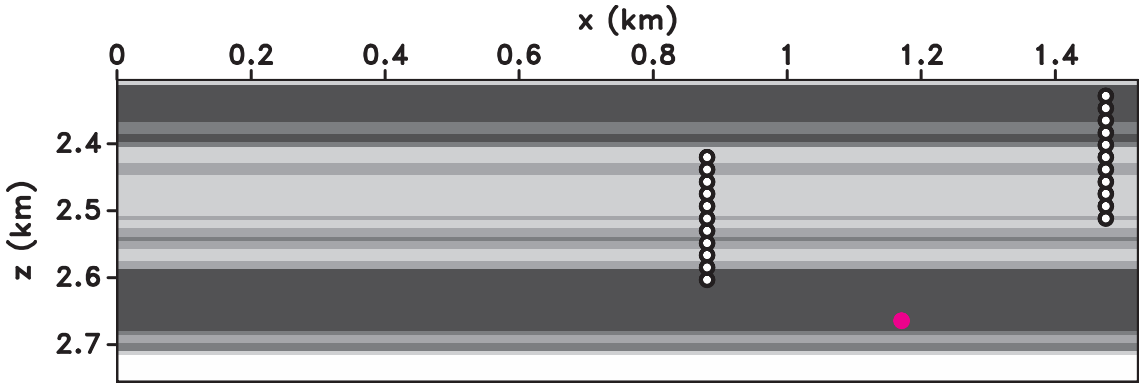


Figure 2.14. Short, dense dual array geometry and velocity model.

There are 20 perforation shots in the case study. I choose to forward model the wavefield using the perforation shot in the middle of the dual array, as the arrays record information on both sides of the source. If the source is located outside of the dual array, it is more difficult to develop a definitive focusing of the wavefield, increasing the uncertainties in source location. The wavefield focus is smeared in x and z. Figure 2.15 shows the focusing obtained from the short dual array which is similar to the focusing in both the dual array (Figure 2.11 and Figure 2.13) and the horizontal array (Figure 2.9).

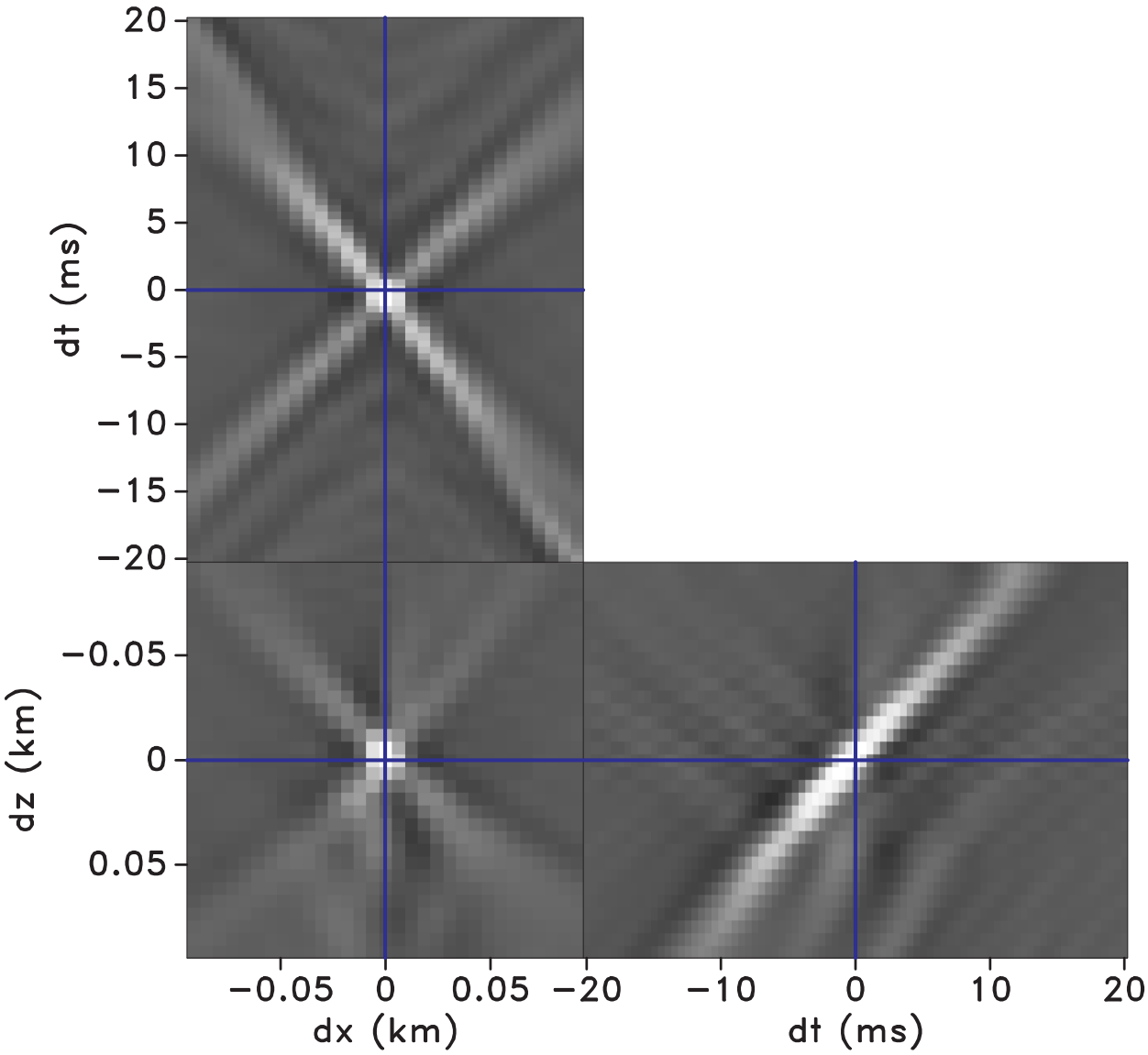


Figure 2.15. Focusing due to a short dense dual array surrounding the source.

The dual arrays sit above the target formation, above the source, similar to the horizontal array in Figure 2.9. Because of this, we cannot resolve the source location as well in the $z-t$ plane. The resolution in the $z-t$ plane is approximately ± 25 m. The source array is, however, located on both sides of the source, laterally, allowing for a better constraint of the focusing in the $x-t$ plane. The resolution in the $x-t$ plane is approximately ± 20 m.

Field data often serve to verify synthetic results. Accordingly, I use field perforation shot data, as in Figure 2.5, to image the source location. Note that the field data are not as clean as the synthetic data; they contain many sources of noise, possess high frequencies, and are elastic in nature (the data contain S-wave arrivals and may possibly contain even anisotropic effects). To use these data, I apply a bandpass filter so that we use only frequencies above 0 Hz and below 200 Hz. I also ignore the elastic properties and focus on the acoustic portion of the data; represented by the p-wave arrivals visible in the field data. The image obtained using the field data is seen in Figure 2.16.

Apart from the phase and presence of noise, the focusing obtained from the synthetic and the field data are in relatively good agreement. The focusing occurs slightly below the correct perforation shot location and is a bit more defocused in the field data than in the synthetic data. This is due to the fact that I forward model and back propagate the synthetic data using the same velocity model, thus there is no timing error in this case. This implies that the synthetic velocity model is true and correct in the synthetic example. This is not the case for the field data example. The model used to back propagate is not the true velocity model that generated the field data. The focusing misplacement in Figure 2.16 makes it apparent that the velocity model used to back propagate the wavefield needs to be updated.

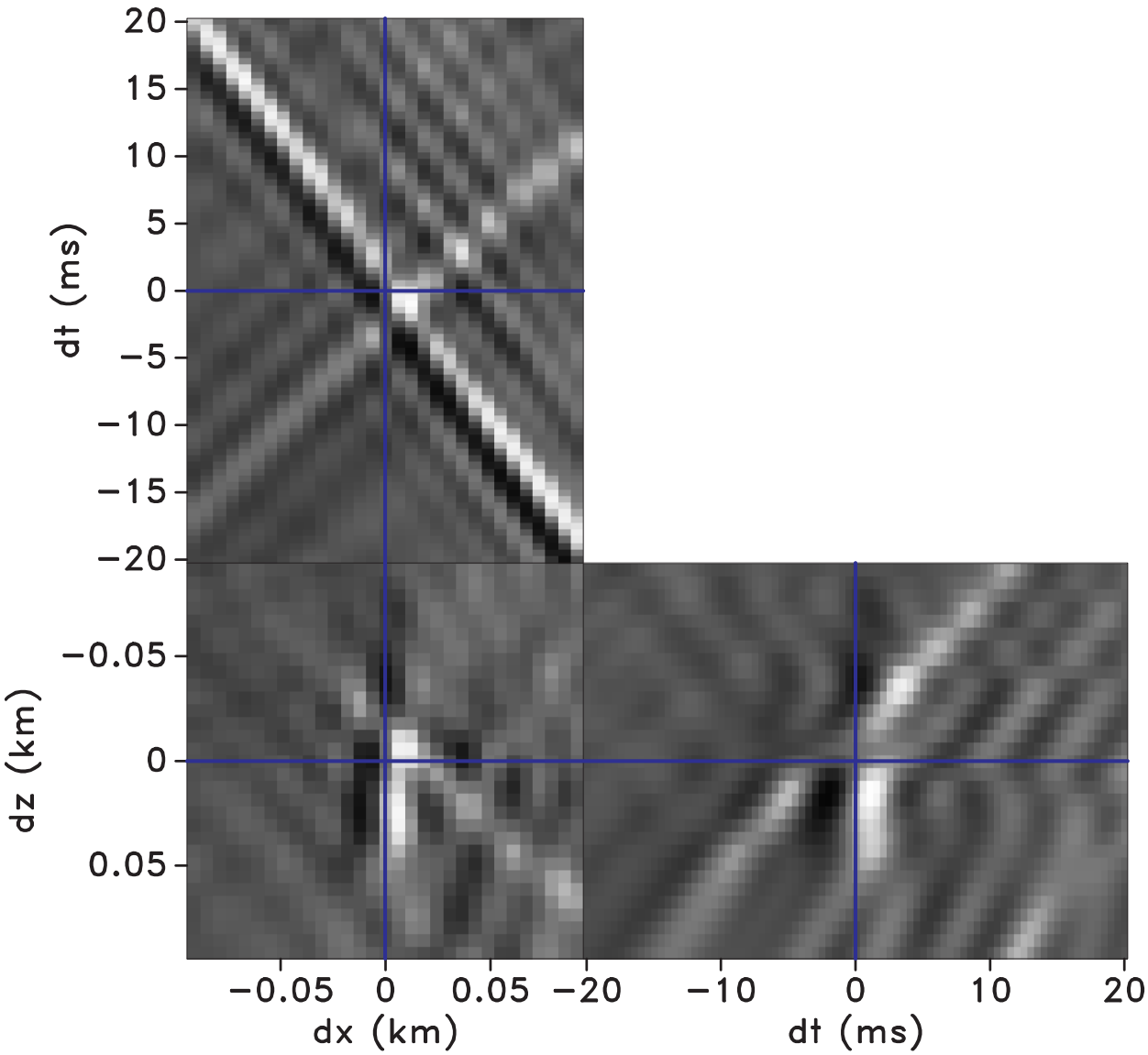


Figure 2.16. Similar to the synthetic example, focusing due to a short, dense dual array using field data.

Dual borehole arrays usually are not available. To understand the effects of a single borehole, I use only one of the vertical monitor arrays to focus the wavefield and compare this focusing with that produced from using both the arrays. The next example uses only the short, dense array on the left, in Figure 2.17.

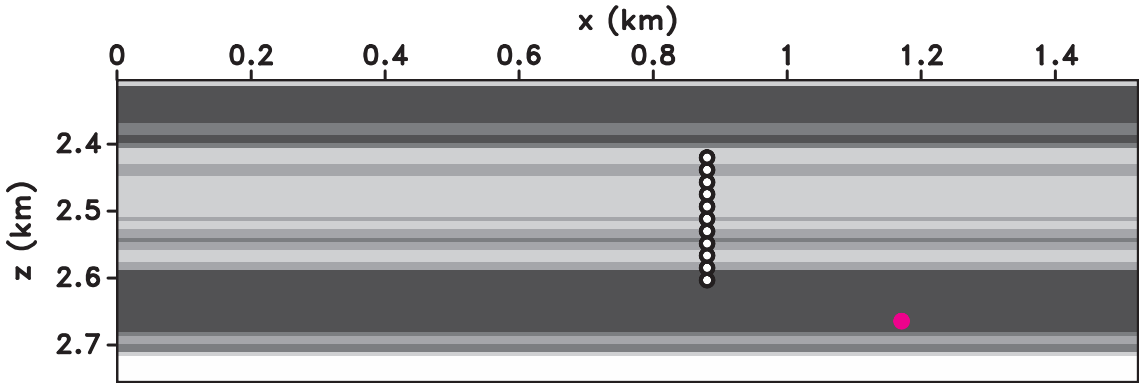


Figure 2.17. Short, dense single array geometry and velocity model.

Given that the short array only receives wavefield information in a limited space above the target, above the source, and on one side of the source only, we expect the focus to be smeared in all planes. There is little information to constrain the focus horizontally or vertically. Figure 2.18 confirms this hypothesis.

The wavefield defocusing in both the $x-t$ and $z-t$ planes extends beyond the panels in the image. The $x-t$ plane contains the most uncertainty in positioning, with a resolution of less than ± 75 m. The $z-t$ plane is better constrained, with a resolution of ± 50 m. The resolution seen in both the $x-t$ and $z-t$ planes is problematic in the case study since the target formation is only 100 m thick. If the source is located along the edges of the target formation, the position smearing due to aperture has the potential to place the source outside of the target formation. Interpreting a source outside of the target formation, when in fact the source is within the formation, leads to misguided decisions regarding stimulation practices, well completions, and reservoir modeling (Hayles *et al.* , 2011).

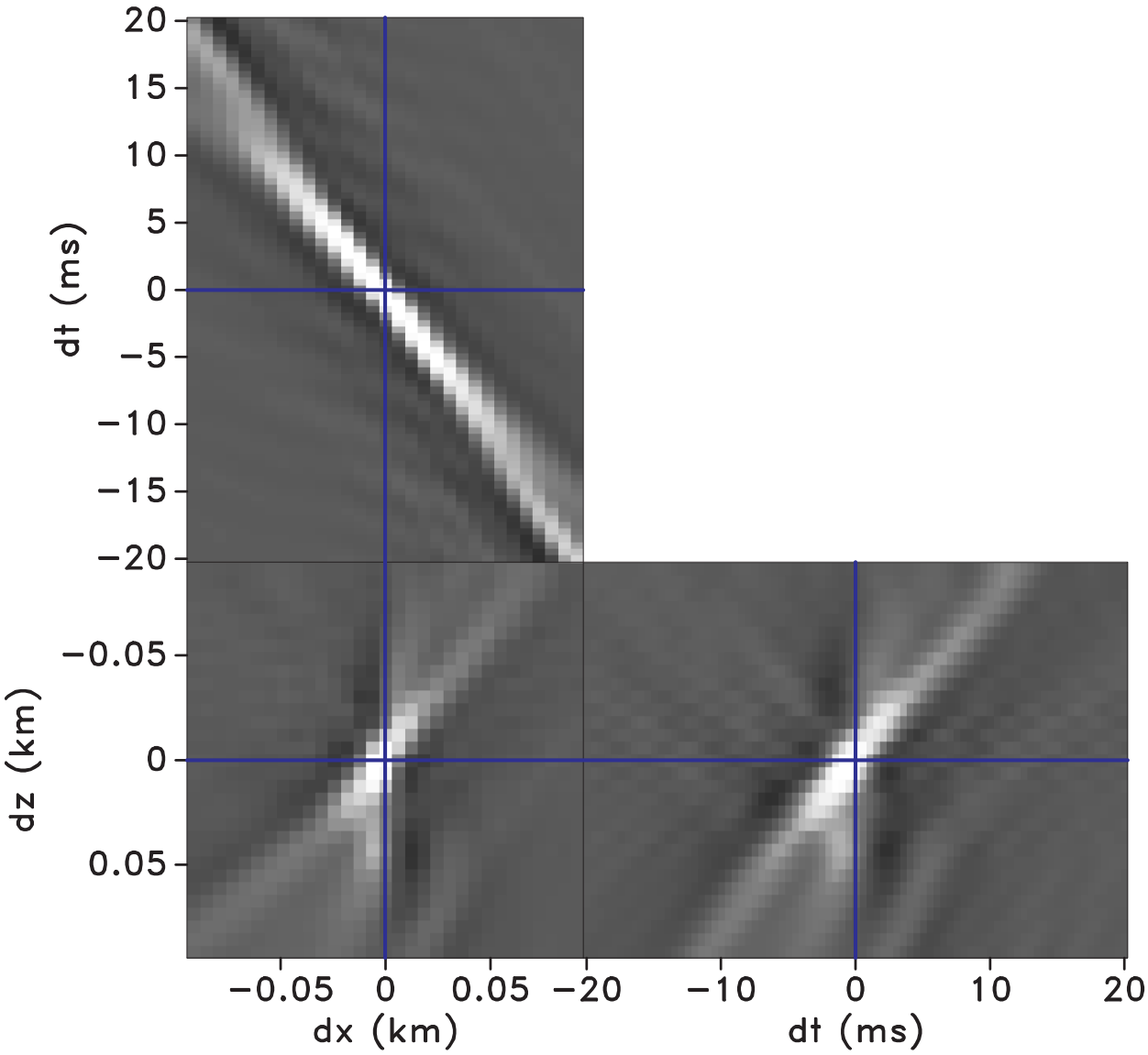


Figure 2.18. Focusing due to a short dense single array above the source.

Figure 2.19 is the focus obtained using field data. Apart from the presence of noise and the phase difference, both the field and the synthetic focusing tend to agree in character quite well. The focusing in the $x-t$ plane in both the synthetic and field examples shows smearing in the wavefield at the source, however the field example places the source location slightly below its correct location (the cross-hairs in all of the panels). The resolution in the $x-t$ plane in the field example is slightly worse than in the synthetic example, which is approximately ± 50 m. The $z-t$ plane focusing is also slightly worse in the field example: more than ± 75 m and extends beyond the display panel of the image.

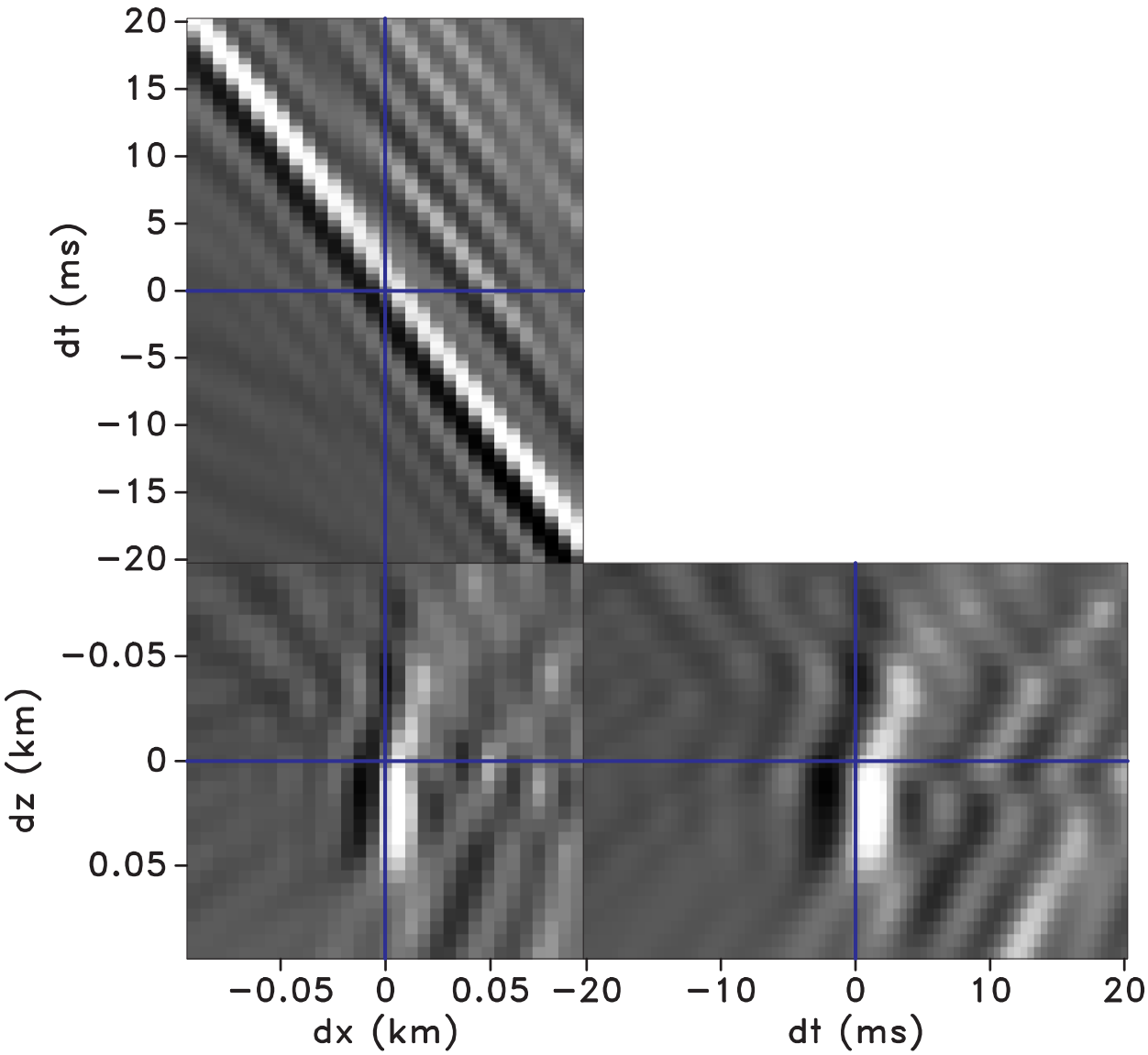


Figure 2.19. Focusing due to a short dense single array above the source and target formation using field data.

2.3 Conclusions

I analyze several different array geometries ranging from an ideal, yet unrealistic, full-aperture array to a more typical short receiver array with severe limitations in aperture. Based on the sequence acquisition geometries, I can conclude that the longest array available to industry should be deployed in vertical wells, as the longer arrays straddle the target formation and source, producing a better wavefield focus of the event.

Long receiver arrays are not presently common in industry for multiple reasons. Most vertical arrays reside in wells that already exist and these wells typically do not extend beyond the depth of the target formation. To drill a few hundred extra feet in a well that already exists, simply for a monitoring exercise, is costly. Given that microseismic processing is still in the early stages, the benefit of drilling to extend an existing well does not outweigh the cost and is difficult to justify. Similarly, it is not cost-effective to drill an entirely new well simply for the purpose of increasing aperture in a monitoring exercise. However, it is important to note that accuracy and precision are of high priority in microseismic monitoring. Herein lies a conundrum: If accuracy and precision are of high priority in microseismic monitoring, why then are measures not being taken to increase the aperture of the acquisition? We know that acquisition aperture increases the information recorded, and in turn, increases the ability to accurately and precisely focus the wavefield and locate microseismic events.

Chapter 3

FINDING THE SOURCE ONSET TIME

Adequate wavefield focusing has three requirements: (1) sufficient aperture, (2) knowledge of the correct source onset time, and (3) a true and accurate velocity model. Using the case study geometry, I explore the effects of not knowing the source onset time and develop a method to correct timing ambiguities. In order to be able to make onset time corrections, we must assume that the velocity model used to propagate the wavefield has the same mean ad the true velocity model.

3.1 Introduction

Source onset time and velocity possess a reciprocal relationship that severely limits the ability to update a velocity model unless we make critical assumptions about the velocity. If the velocity is incorrect, it is impossible to update the velocity if the source onset time is unknown. Similarly, we cannot find the correct source onset time if the velocity is not correct. Herein lies a processing impasse: How is it possible to update an incorrect velocity model without the knowledge of the source onset time?

To correct for the source onset time we must assume that there is a zero mean difference in slowness between the velocity model used to back propagate the wavefield and the model that generated the data (either in the field or through forward modeling). If this assumption does not hold true, the position of the wavefield focus is mislocated by both incorrect time and incorrect velocity. With assumption that the model used to propagate the data has the same mean as the true velocity model, an incorrect velocity model simply defocuses the microseismic wavefield rather than mislocating the focus. Correcting for source onset

time without making the zero mean slowness assumption results in erroneous velocity model updates and event positions.

Assuming that the mean slowness difference between the velocity model used to propagate the wavefield and the true velocity model is zero, I continue with the methods implemented in Chapter Two. I use the single receiver array and velocity model seen in Figure 2.17 as well as the known perforation shots to investigate the issue of source onset time, as the position in space is known.

Using the definition of an image described in Chapter Two, we analyze the focusing of the wavefield when the source onset time is unknown. If the source onset time is incorrect, i.e., not at time zero, the focusing in space occurs at an incorrect location. To correct for the focusing of the wavefield at the incorrect location in space, we simply shift the focus in time so that it occurs at time zero, the onset time of the source.

A method for determining the source onset times already exists based on picking P- and S- first break arrivals. Recall, however, that picking arrival times on field data can be tricky in the presence of noise or a severely limited acquisition aperture (Bose *et al.* , 2009). In lieu of picking arrival times on the data, I advocate picking times of focusing from the wavefield. Picking on the wavefield allows detection of events which might have been masked by noise, even low amplitude events which would otherwise have gone unnoticed. The methods for locating microseismic events in industry are heavily reliant upon the first-break P- and S- arrival picks. If one does not pick all of the event arrivals in time then the microseism location algorithm produces higher uncertainties in event positioning. These uncertainties are eliminated by picking focusing on the wavefield rather than onset times on the data.

3.2 Finding the source onset time: a synthetic example

My case study data detailed in the proceeding chapters do not contain any information regarding the source onset time. In addition, the data recorded in each wellbore are in no way correlated with one another in either absolute or relative time. If the data were correlated in time so that they have the same time reference, we obtain information about the velocity variations given the known source and receiver positions. Unfortunately this is not the case. To be able to update the velocity model, the source onset time must be determined.

The experiment begins by forward modeling synthetic data and then shifting them in time by some arbitrary amount, which simulates a situation where we do not know the source onset time. (For example, a contractor may present a dataset where the onset time of a perforation shot was not recorded and is unknown.) Given the synthetic data with an incorrect time reference, the wavefield slice in space and time produces an image with a focus at the incorrect position in space. Figure 3.1 is an example of an incorrectly placed focus caused by not knowing the correct source onset time. The synthetic microseismic wavefield does not focus at the correct location in space and time. The misplacement of the focus in x and z is approximately 50 m and 25 m, respectively. Once we identify a focus, we apply a shift in time so the wavefield focus occurs at time zero. Unfortunately, it is unclear from the three-dimensional image what the shift in time needs to be in the wavefield so that we shift the focus to time zero. To improve our understanding of focusing in time, I develop a subsidiary image where we examine the focusing in time in a one-dimensional space: I eliminate the spatial variables allowing only time to be seen. We explore a single point in space at the correct source location, in this case $x = x_{shot}$ and $z = z_{shot}$. At this single location in space, we observe the focusing with respect to time only in Figure 3.2.

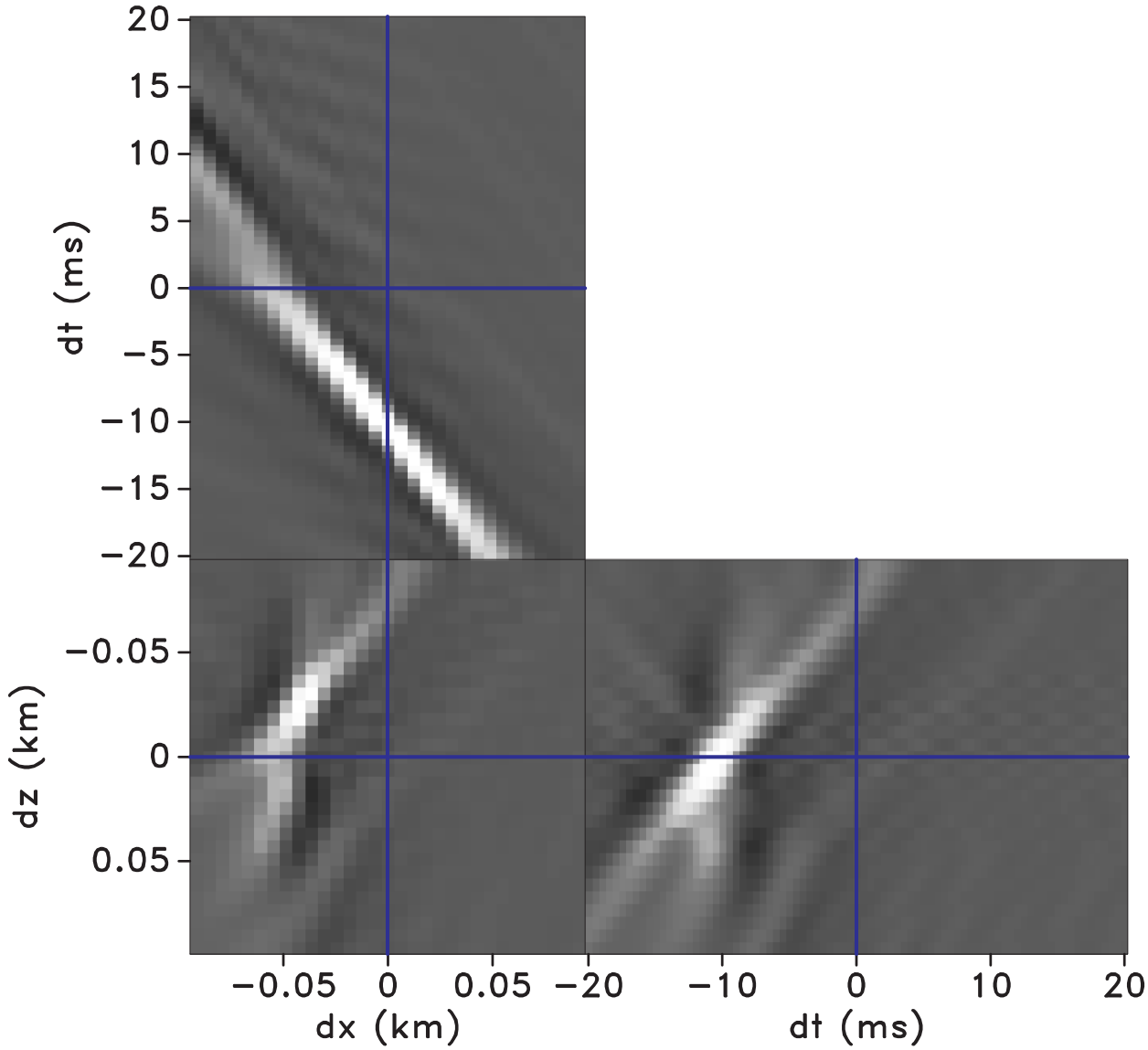


Figure 3.1. An incorrect source onset time does not allow the wavefield to focus at the correct position in space or time.

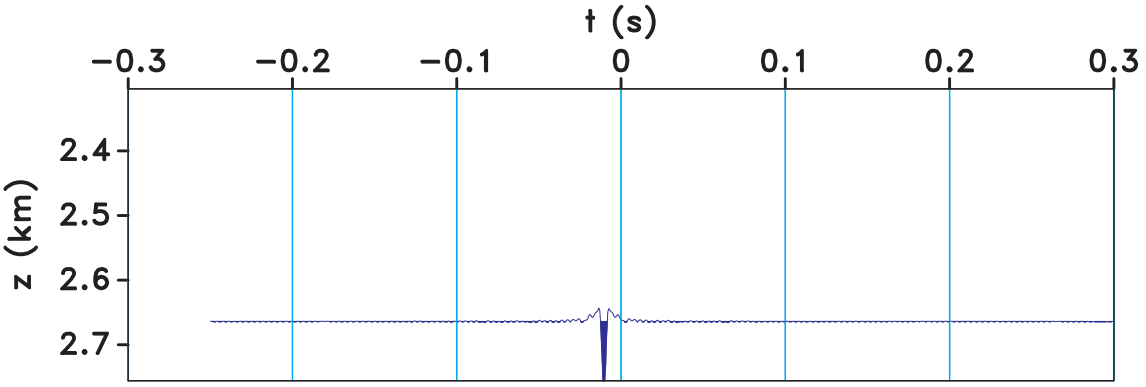


Figure 3.2. Time of focusing at the source location in space with respect to time, when the source onset time is non-zero.

The z-axis in Figure 3.2 acts simply as visual place-holder for the reader indicate the source location in depth; it has nothing to do with the misplacement of the source in space due to incorrect source timing measurements. The single peak on the time axis, observed around approximately -0.01 s, is the wavefield focus.

If the wavefields are noisy or it is difficult to determine the time of the wavefield focus, I recommend applying cross-correlation to determine the appropriate time shift needed so that the source occurs at time zero. To do this, I cross-correlate the observed and calculated wavefields at the source location using this expression:

$$CC_1 = W^{cal}(\mathbf{x}_{source}, t) \star W^{obs}(\mathbf{x}_{source}, t), \tag{3.1}$$

where CC_1 is the cross-correlation at the source location, W^{cal} is the calculated wavefield, W^{obs} is the observed wavefield, $\mathbf{x}_{source}$ is the source position in space, and t is time. Figure 3.3 shows the cross-correlation of the wavefields at the source location in space.

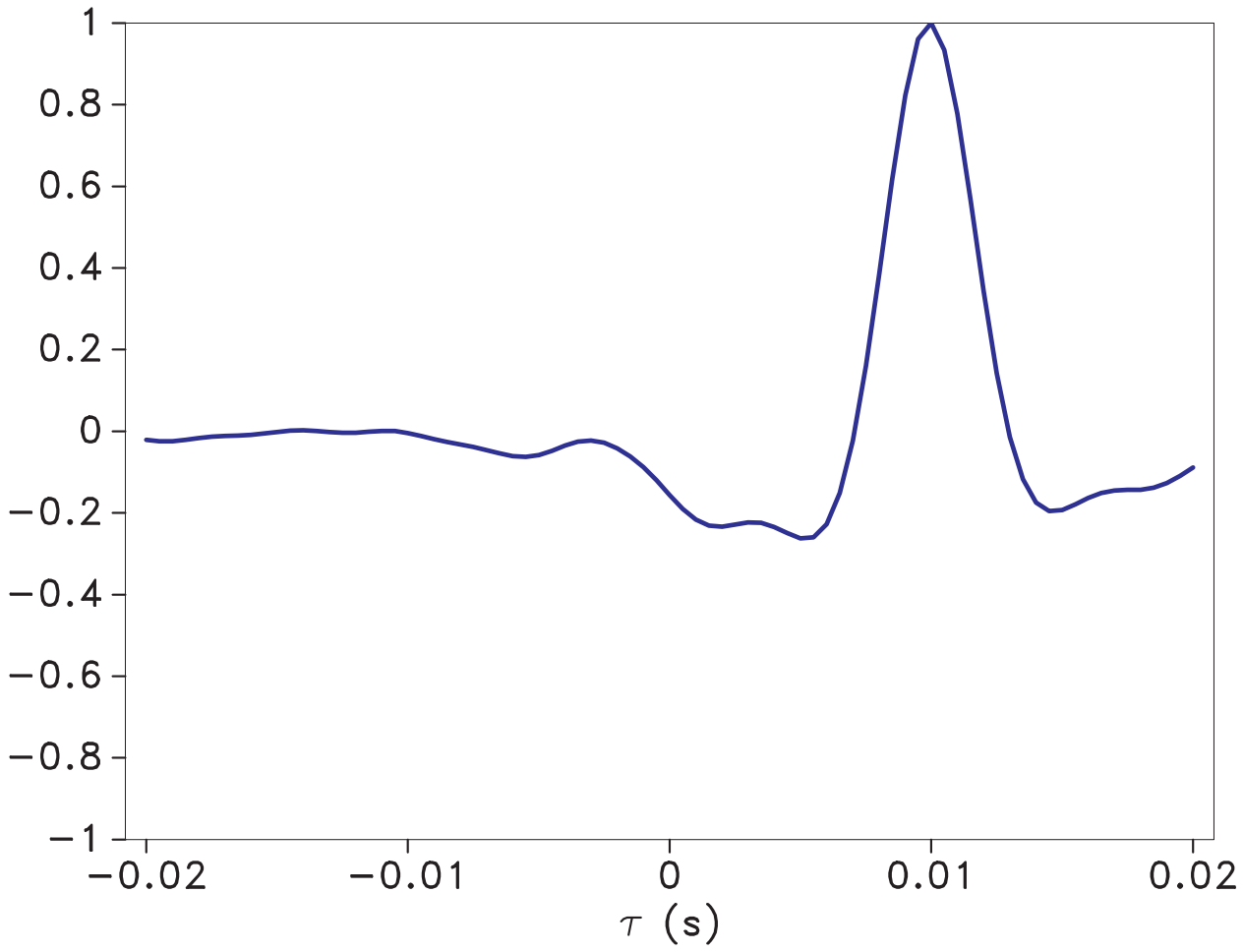


Figure 3.3. Cross-correlation between the observed (incorrect onset time) and calculated (correct onset time) wavefields at the source position in space.

The peak of the cross-correlation occurs at 0.01 s, the amount of time needed to shift the wavefield so that the source occurs at time zero. In this synthetic case, the observed wavefield W^{obs} is the wavefield propagated with an incorrect onset time. The calculated wavefield W^{cal} is the same wavefield, but with a correct onset time.

Equation 3.1 inspects the cross-correlation at the source location only and does not include all information spatially. To include all of the spatial information in the cross-correlation, I stack over the spatial variables, x and z.

$$CC_2 = \sum_{\mathbf{x}} W^{cal}(\mathbf{x}, t) \star W^{obs}(\mathbf{x}, t), \tag{3.2}$$

where CC_2 is the cross-correlation stacked over all spatial variables. Again, the observed wavefield W^{obs} is the wavefield propagated with an incorrect onset time and the calculated wavefield W^{cal} is the same wavefield with the correct onset time. Figure 3.4 shows the cross-correlation of the two wavefields stacked over space.

As expected, the peak of the cross-correlation in Figure 3.4 occurs at 0.01 s. The peak, however, is wider in the stacked cross-correlation curve seen in Figure 3.4 than seen in the cross-correlation curve taken at the source location seen in Figure 3.3. Regardless, both peaks occur at the same time. Using the time at which the cross-correlation peak occurs, I apply a time shift in the wavefield so that the source occurs at zero time, seen in Figure 3.5.

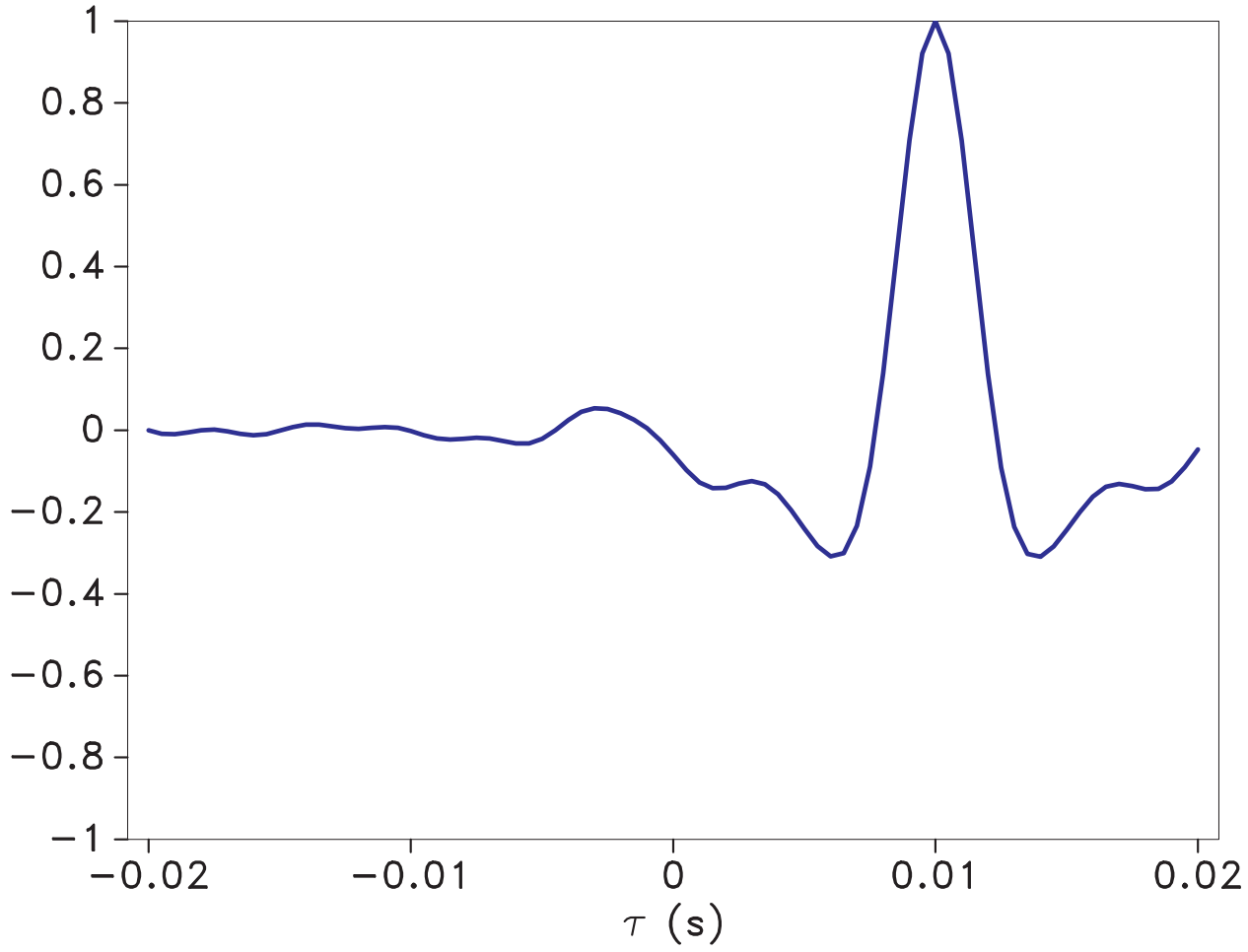


Figure 3.4. Cross-correlation between the observed (incorrect onset time) and calculated (correct onset time) wavefields tacked over space.

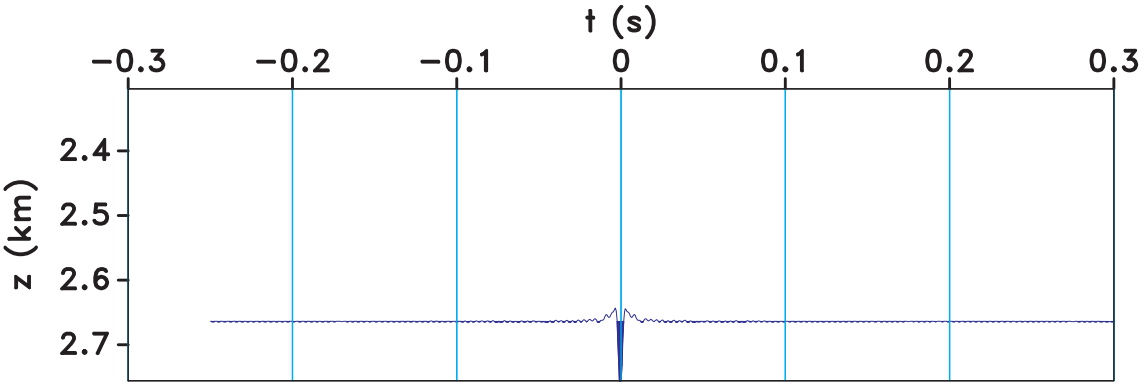


Figure 3.5. Synthetic example: Time of focusing at the source location in space and time, occurring at a non-time zero.

Notice that the time difference between the wavefield focus at the incorrect and correct times is small, approximately 0.01 s. In reality, this time difference is typically greater than what we observe in this synthetic example. Interestingly, such a small time difference produces a large positioning error in space as seen in Figure 3.1. A correct onset time of the source translates to a correct positioning of the source in space. Once we shift the focus so that it occurs at time zero, we expect that the focus in space is also located at the correct position. Figure 3.6 is the corrected wavefield focus in space and time.

Shifting the wavefield in time so that the focus occurs at time zero, as expected, shifts the focus to the correct source location in space. The focus caused by the incorrect source onset time in Figure 3.1 is misplaced by approximately 50 m in x and 25 m in z, and the time difference is only 0.01 s! Imagine if the source onset difference is greater than 0.01 s; the source positioning is also greater in space. A misplacement of the source by more than ± 50 m has the potential to be identified outside of the target formation, resulting in erroneous interpretations of the fracture network.

Next, I present an example using field data contaminated by noise with the purpose of validating the findings regarding source onset time.

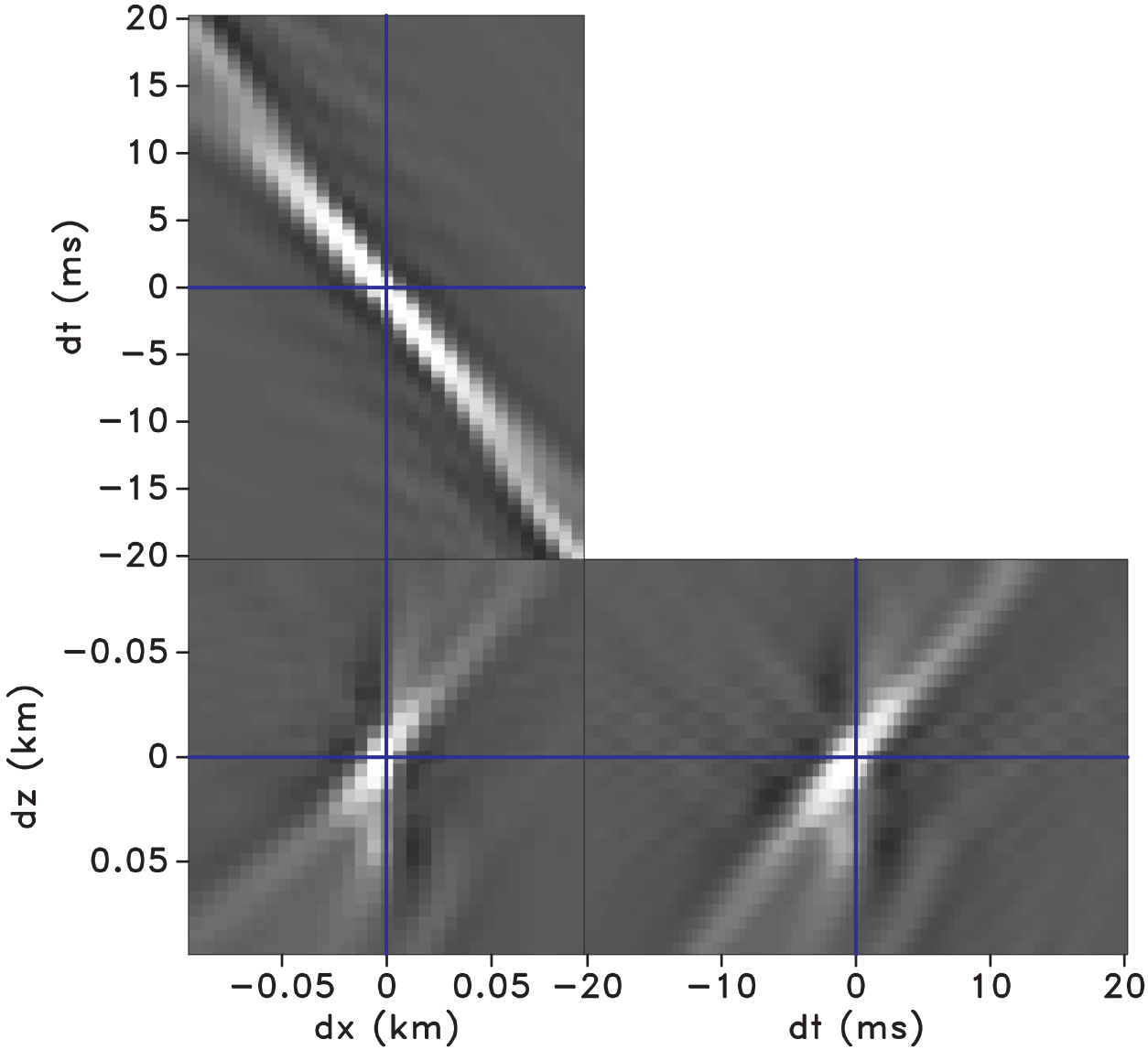


Figure 3.6. Focusing in space and time at the source location, corrected so that the source onset time is at time zero.

3.3 Finding the source onset time: a field example

Previously I argued that it is difficult to pick events on noisy data such as field data. The question then arises: Why do I advocate picking events on a wavefield instead of picking arrivals on data? It appears that picking events on a wavefield contaminated by noise is just as difficult as picking first-break arrivals on noisy data. I advocate picking on the wavefield because the wavefield captures more information about the source in space and time than given by simply data time-picks. The wavefield captures source frequencies, amplitudes, and timing measurements whereas time-picks simply include time information. In addition, events otherwise masked by noise in the data are focused in the wavefield. In this section I present a field example that supports my decision to pick on the wavefield rather than on the data.

The field example source-receiver array geometry is identical to the synthetic example. My case study data lacks information about the source timing of the perforation shots. This implies that each dataset from each wellbore needs to be corrected so that the source onset time occurs at time zero. To be able to proceed with velocity model updating in the next chapter, the source onset time is a critical piece of information and must be known.

Figure 3.7 shows the focusing in space using field data due to an unknown source onset time. In this particular example we do not know the source onset timing. The data are provided by the contractor in partitioned segments of 15 s, each with a time sampling rate of 0.5 ms. The first-break arrival could occur at any time within the 15 s time window. To reduce the computing time, I inspect the data and cut the 15 s time intervals down to 5 s. The only criteria for this cutting process is that the 5 s time window must include wavefield information, such as a P-wave arrival. Otherwise, it does not matter where the time window begins or ends.

Similar to the process described in the synthetic example, I restricted the focusing of the wavefield to the exact location of the source in space, which allows us to investigate the focus with respect to time only. Figure 3.8 shows the focus using the field data. Just as in

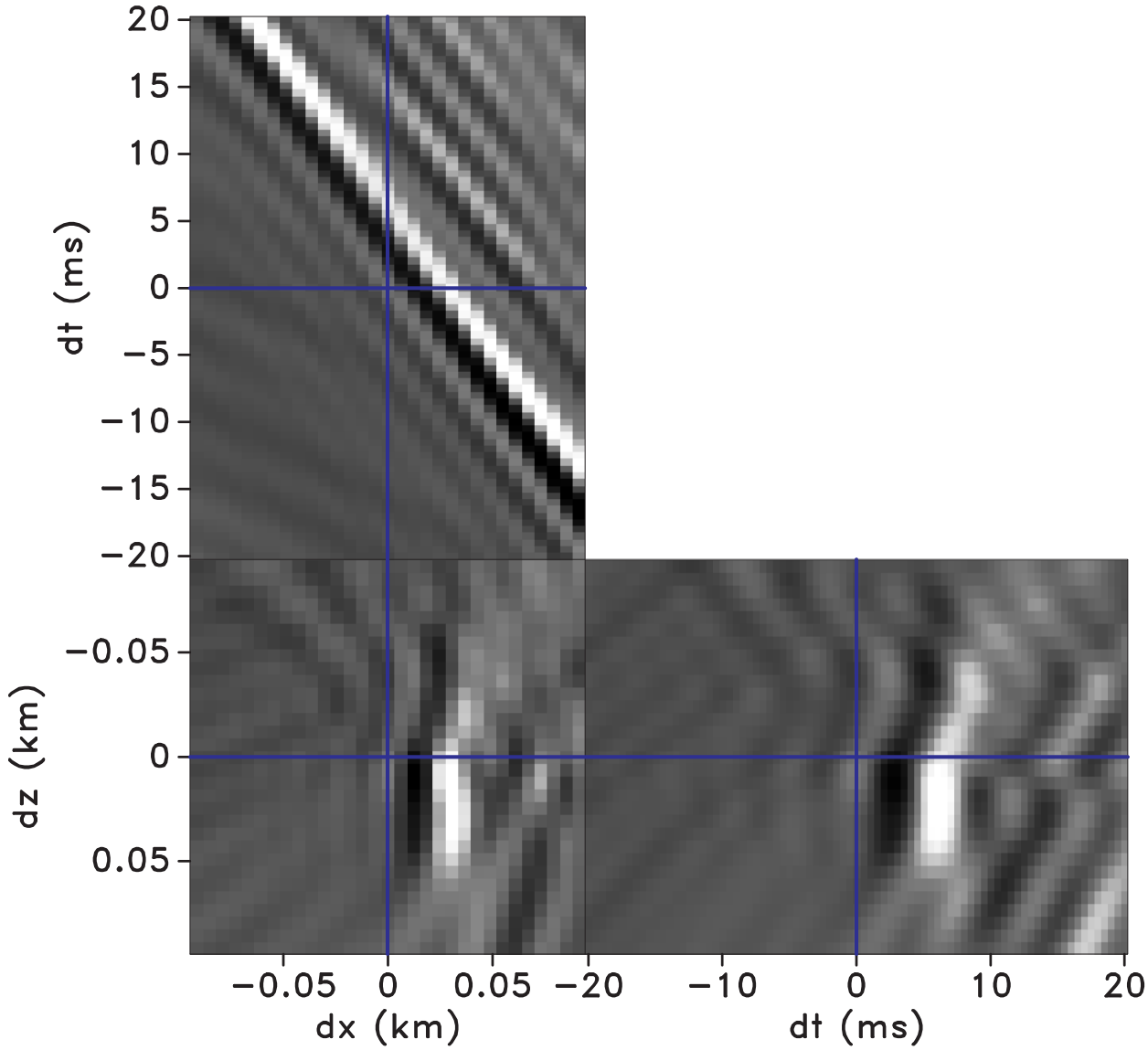


Figure 3.7. An incorrect source onset time does not allow the wavefield to focus at the correct position in space or time.

the synthetic example shown in Figures 3.2 and 3.5, the z-axis is only intended to be used as a reference to the true source location in depth and should not be considered a vertical measurement of the source misplacement in depth.

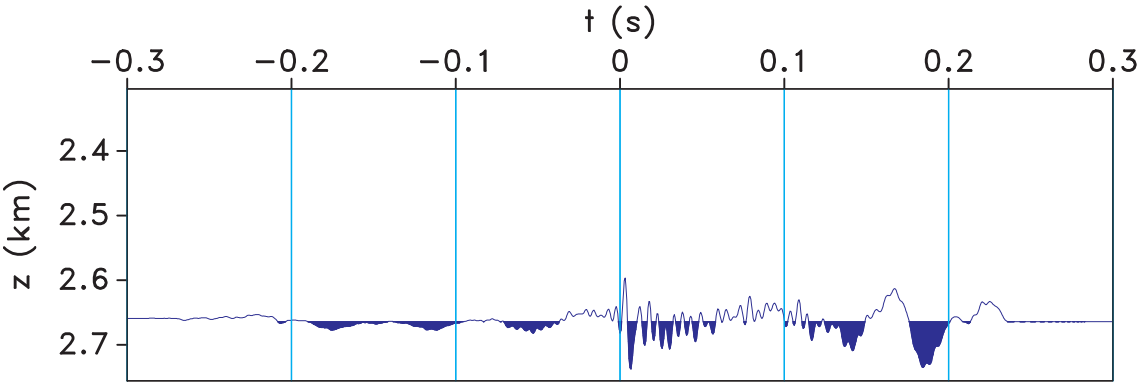


Figure 3.8. Synthetic example: Time of focusing at the source location in space and time, occurring at a non-time zero.

We are unable to determine the time of the focus because the data are contaminated with noise. The highest amplitude and highest frequency peak in the wavefield is the focus located at approximately 8 ms. The peak located at approximately 0.16 s appears to be noise. Shifting the wavefield by approximately 8 ms in time moves the wavefield focus so that it occurs at time zero.

Similar to the process used with the synthetic example, I apply cross-correlation to determine the time shift needed so that the wavefield focuses at time zero. I cross-correlate the observed wavefield W^{obs} (field) with the calculated wavefield W^{cal} (synthetic) at the source location seen in Figure 3.9. The peak of the cross-correlation occurs at -8 ms, the amount of time needed to shift the wavefield so that the focus occurs at time zero.

So that we include all of the spatial information in the cross-correlation curve, I stack over all spatial variables seen in Figure 3.10. As expected, the peak of the curve occurs at the same time as the curve seen in Figure 3.9, -8 ms.

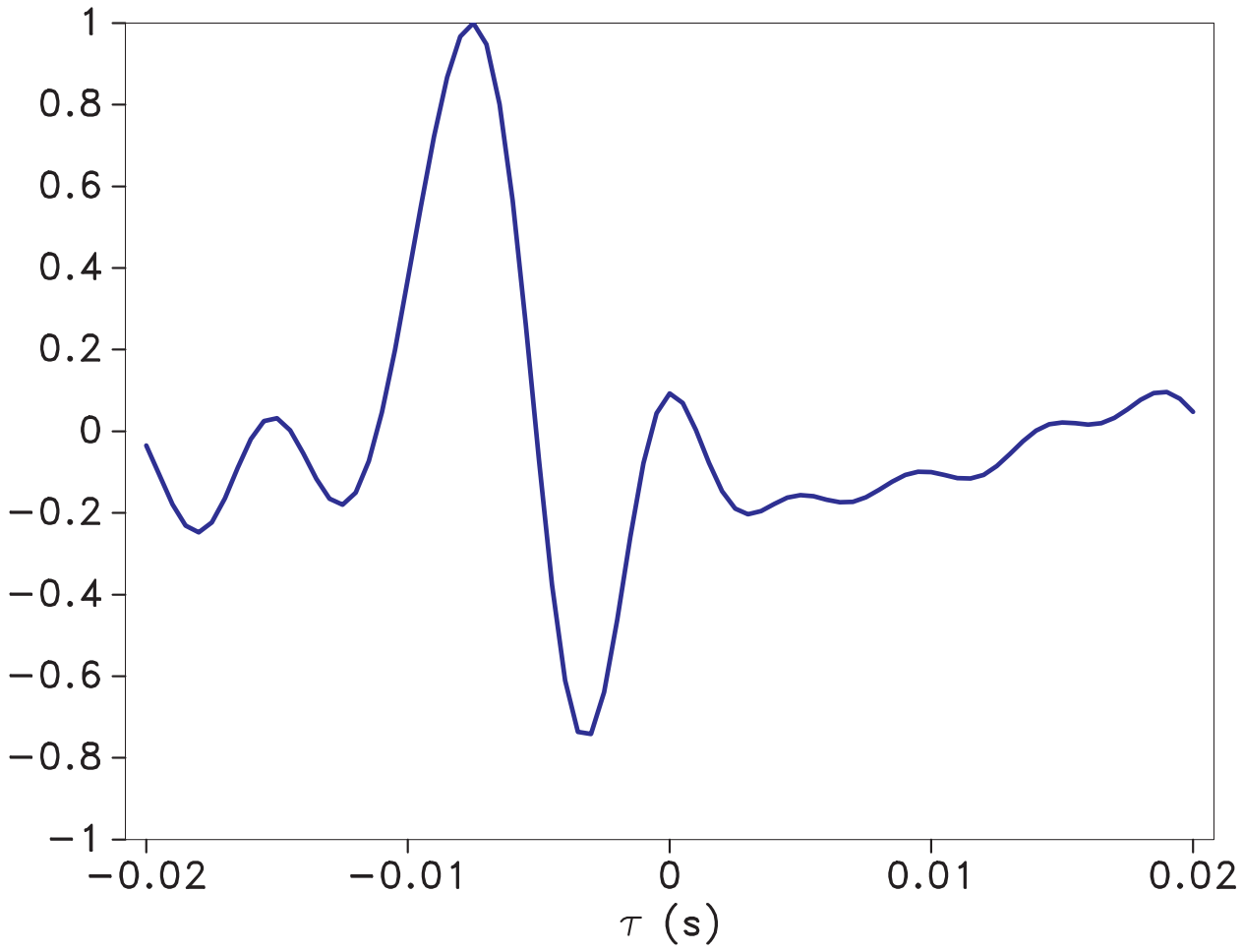


Figure 3.9. Cross-correlation between the observed (field) and calculated (synthetic) wavefields at the source position in space.

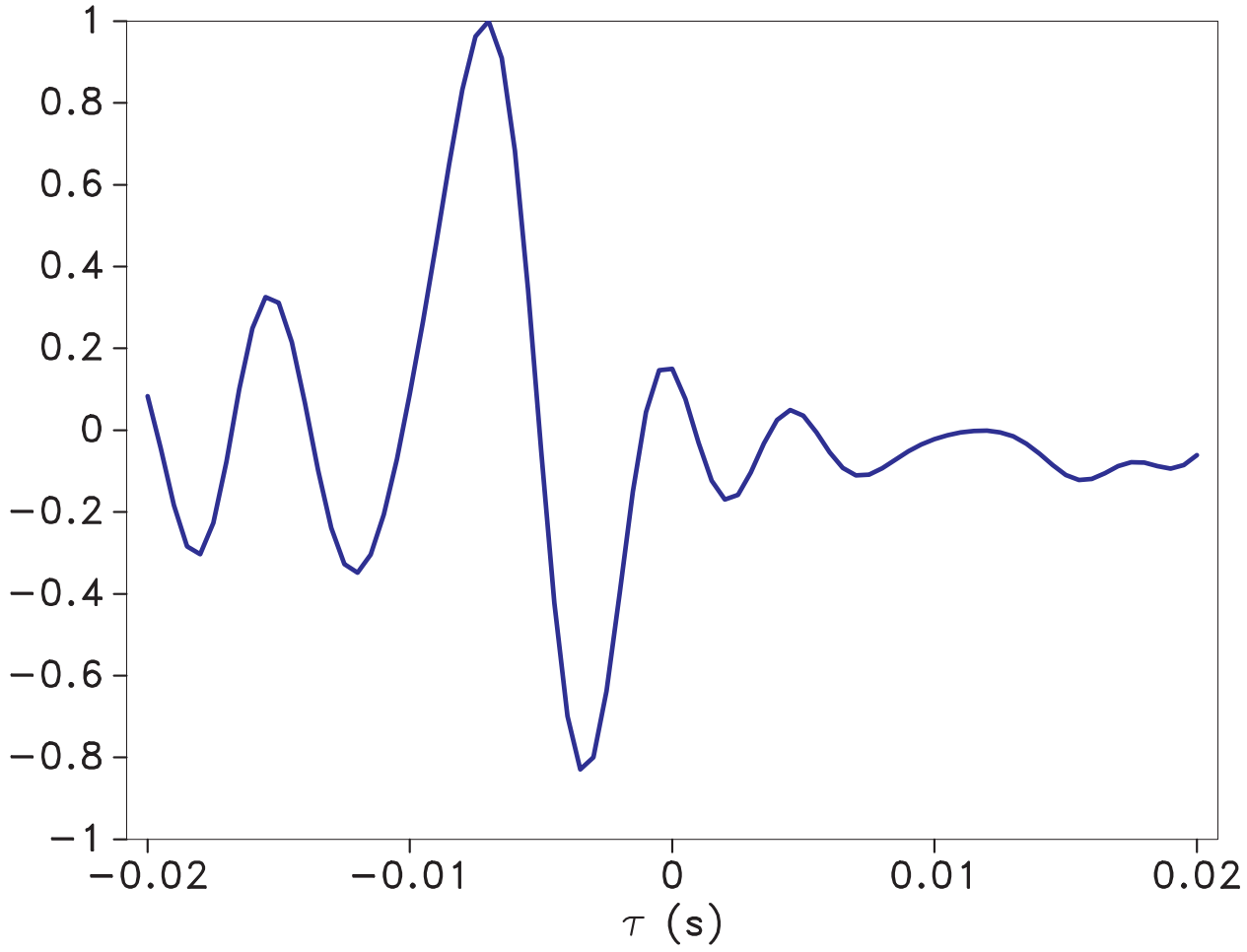


Figure 3.10. Cross-correlation between the observed (field) and calculated (synthetic) wavefields at the source position in space.

Using the time at which the cross-correlation peak occurs, I apply an -8 ms time shift to the wavefield. The highest frequency and highest amplitude peak, or wavefield focus, seen in Figure 3.11 now resides at time zero. The three-dimensional slice in the wavefield, shown in Figure 3.12, illustrates that the applied time shift is indeed correct. Notice that a time shift of -8 ms moved the source focus in space by 25 m in x. More often than not, the time discrepancy seen in the field data is much larger that 8 ms. This time difference translates to a mislocation of the focus of more than ± 25 m in x.

Similar to the synthetic example, the incorrect source onset time misplaces the focus. Such a discrepancy between the time of the occurrence of the wavefield focus and time zero is common in field data and needs to be corrected before one implements any velocity inversion or source location techniques.

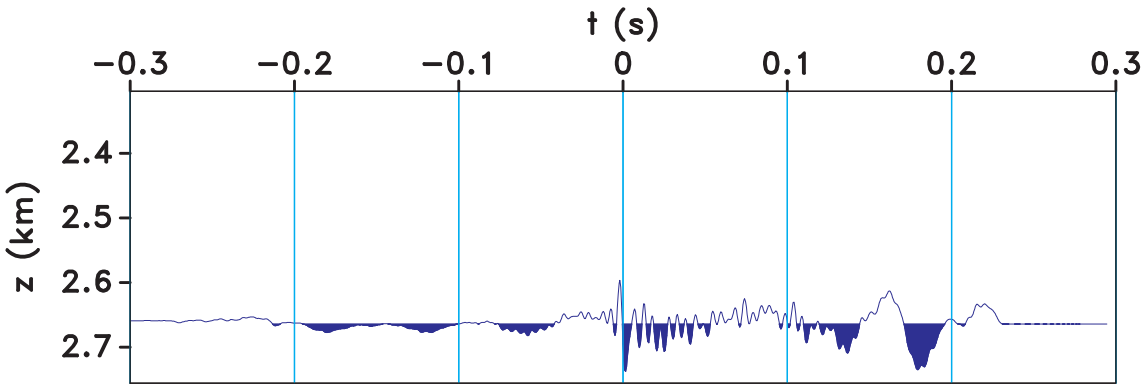


Figure 3.11. Synthetic example: Time of focusing at the source location in space and time occurs at a non-time zero.

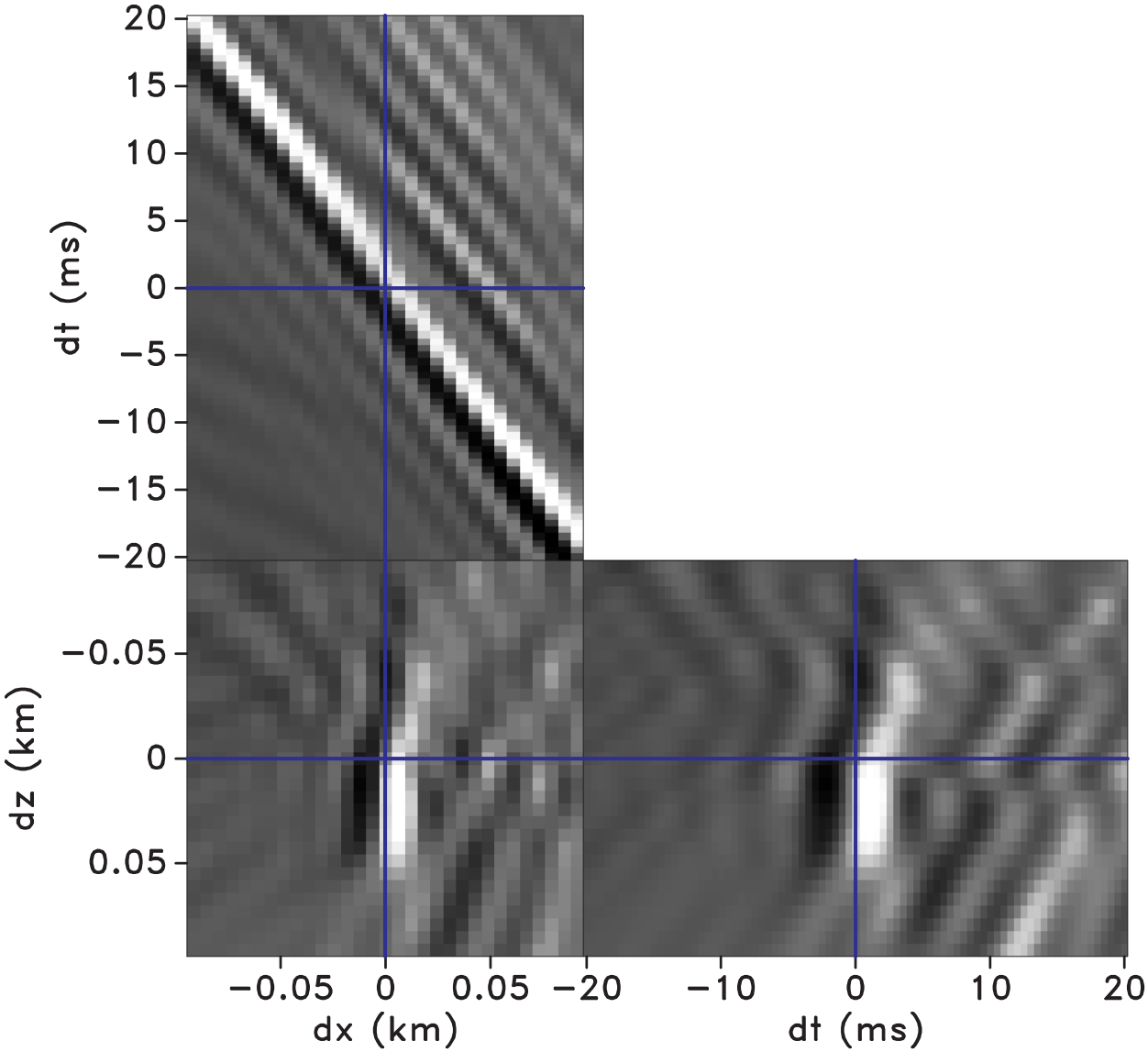


Figure 3.12. Focusing in space and time at the source location, with corrected time so that the source onset time is at time zero.

3.4 Conclusions

In order to be able to correctly position the source in space, we must know the onset time. Unfortunately, onset time is information that field microseismic data typically do not contain. To be able to proceed with velocity model updates, the source position in time and space must be as accurate as possible. To correct for the source onset time, we shift the wavefield focus in time so that it occurs at time zero. Through investigating the three-dimensional cube slices as well as the time-slices around the source location, we correct both synthetic and field data examples for an unknown source onset time. The final wavefield focus occurred at the correct location in space and time after we apply the onset time correction.

Chapter 4

EFFECTS OF INCORRECT VELOCITY ON WAVEFIELD FOCUSING

Using the case study geometry and assuming that the adjusted source onset time is correct, I conduct forward modeling of the wavefield in order to understand the behavior of focusing given incorrect velocity models. In the subsequent sections I present three different velocity model scenarios and compare the wavefield focusing of each to that obtained from the true velocity model. Comparing the true and calculated wavefields both in the data- and image-domain, I explore the applicability of using waveform tomography (WET) to update a velocity model.

4.1 Introduction

Most microseismic processing techniques use a simple one-dimensional velocity model with the assumption that this model correctly characterizes the observed events. If the starting model does not correctly reposition known sources (e.g., perforation shots or string shots) to their true location, one typically uses a combination of ray-tracing, least squares optimization, and grid search to update both the hypocenter locations and the velocity model (Thurber, 1992; Abel, 2011). Since I apply the two-way wave equation rather than ray-tracing to locate events, I advocate the use of wavefield tomography to update velocity models. I formulate an objective function that relates the wavefield focusing to the velocity perturbations in both the data- and image-domain. In both cases, I make use of the entire observed data, instead of picked events as is the case with travel-time tomography.

Before I delve further into the methods of velocity model updating, we need to develop a solid understanding of how a perturbed velocity model affects the accuracy of wavefield

focusing around a point source in space and time. To illustrate the effects of incorrect velocity on wavefield focusing, I present three scenarios. Continuing with the same modeling techniques used in the previous chapters, I implement the two-way wave equation using slow and fast mean velocity models, and a smoothed zero-mean velocity model. I inspect the wavefield around the point source in both space and time in all three scenarios, and assess the quality and characteristics of the wavefield focusing. This experiment assumes that I know the source position and trigger time, as is the case for perforation shots.

4.2 Effects of Incorrect Velocity on Wavefield Focusing

We established in previous chapters that acquisition aperture and incorrect source onset timing smear and misposition the wavefield focus, respectively. In this chapter I hold the acquisition aperture and timing measurements constant by only using the case study acquisition geometry and by assuming that the source onset time is correct. I then conduct a wavefield experiment with the purpose of understanding the focusing due to a slow, fast, and smoothed velocity model.

4.2.1 Case Study

Using the two-way acoustic wave equation, I forward model the wavefield with the velocity model shown in Figure 4.1 as the base model. I inspect the wavefield at the location of the source, in this case located between the two monitor arrays at $x = 0.88$ km and $x = 1.47$ km, respectively, in order to assess the quality of wavefield focusing.

In Chapter Three, I have assumed that the velocity model used to propagate the wavefield must have a zero-mean slowness difference from the true model. This assumption is critical because a slow or fast velocity in combination with an incorrect onset time misplaces the wavefield focus in both space and time. It is difficult to distinguish between velocity and incorrect timing as the ultimate cause of the wavefield focus misplacement. A zero-mean difference in theory eliminates the possibility of wavefield focus misplacement due to

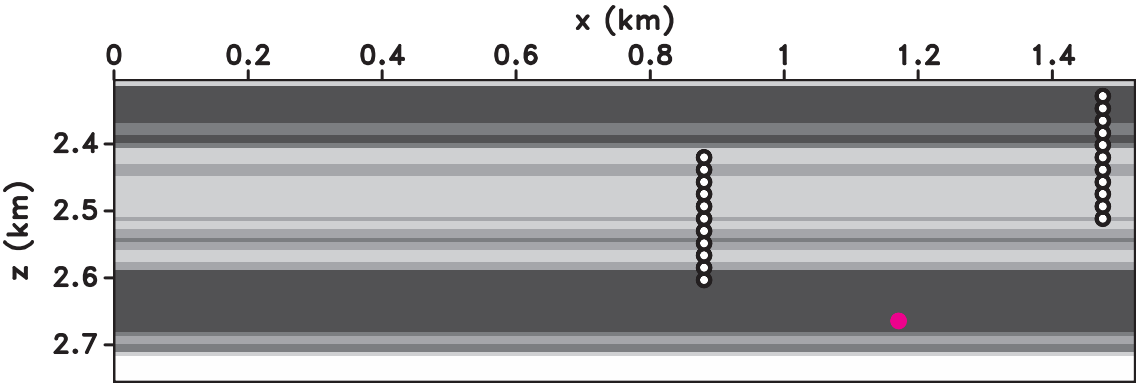


Figure 4.1. True velocity model.

incorrect velocities. Assuming a zero-mean difference, we expect the wavefield focus to be slightly defocused yet correctly positioned. Figure 4.2 illustrates this expectation.

The focusing seen in Figure 4.2 obtained from the zero-mean smooth model is defocused compared to the focusing seen in Figure 2.15 using the true model. Given the limited array aperture of the case study, the best focusing attainable is still somewhat smeared. The vertical arrays span the source horizontally, constraining the focus in x. However, the arrays are short and reside above the source, providing little constraint in the z dimension. In x and z, the wavefields constructed using data from both boreholes do not completely constructively interfere at the source location. For both the true and smoothed models, the wavefield smears and defocuses producing side-lobes in the focusing image. The focus, however, resides at the correct location in space and time.

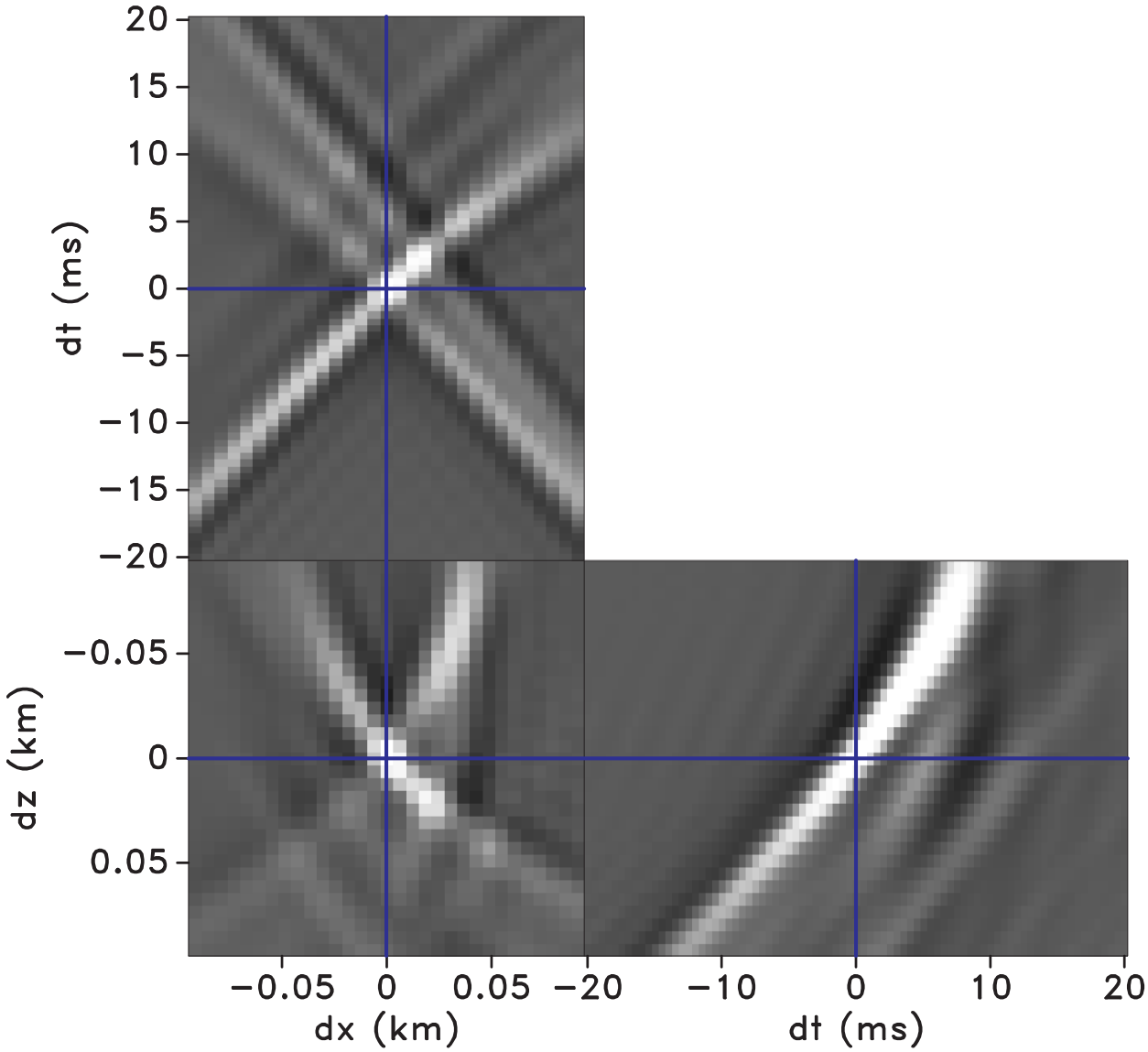


Figure 4.2. Focus obtained using a smoothed, zero-mean velocity model given a short, dual array. The velocity values are the same as seen in Figure 2.3.

Sometimes we do not know if we have a zero-mean velocity model. Perhaps the mean of the starting model is slower or faster than the true model. How then does an incorrect velocity model affect the positioning and degree of focusing in the wavefield around the source? To address this question, I apply an artificial scale to the smoothed model. I create a fast model by scaling the mean slowness by 5%. We expect that the wavefield focus resides below the true location of the source, given that the velocity is too fast. Figure 4.3 shows the defocusing caused by a fast model. As expected, the focus resides below the true location of the source by about 30 m. In addition, the focus is smeared and is nowhere nearly as resolved as the focus obtained from the true model in Figure 2.15.

Similar to the method used to create a fast model, I create a slow model by increasing the mean slowness by 5%. Using the slow model to propagate the wavefield, we expect the focus to reside above the true location of the source, with a poorer spatial and temporal resolution compared to the true model focusing in Figure 2.15. Figure 4.4 shows the wavefield focusing due to propagating the wavefield in a slow model.

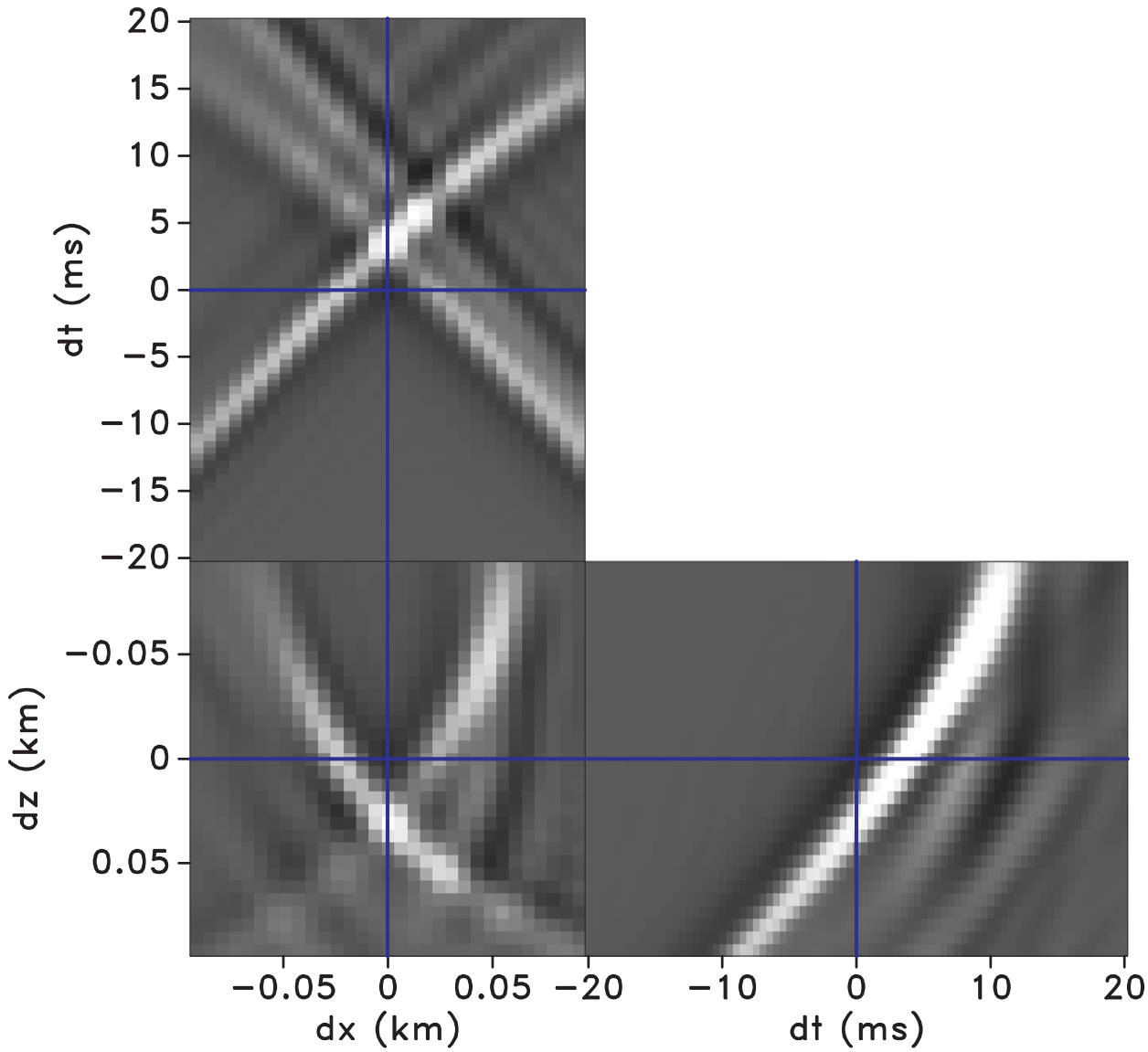


Figure 4.3. Focus obtained using a fast velocity model given the case study geometry shown in Figure 4.1.

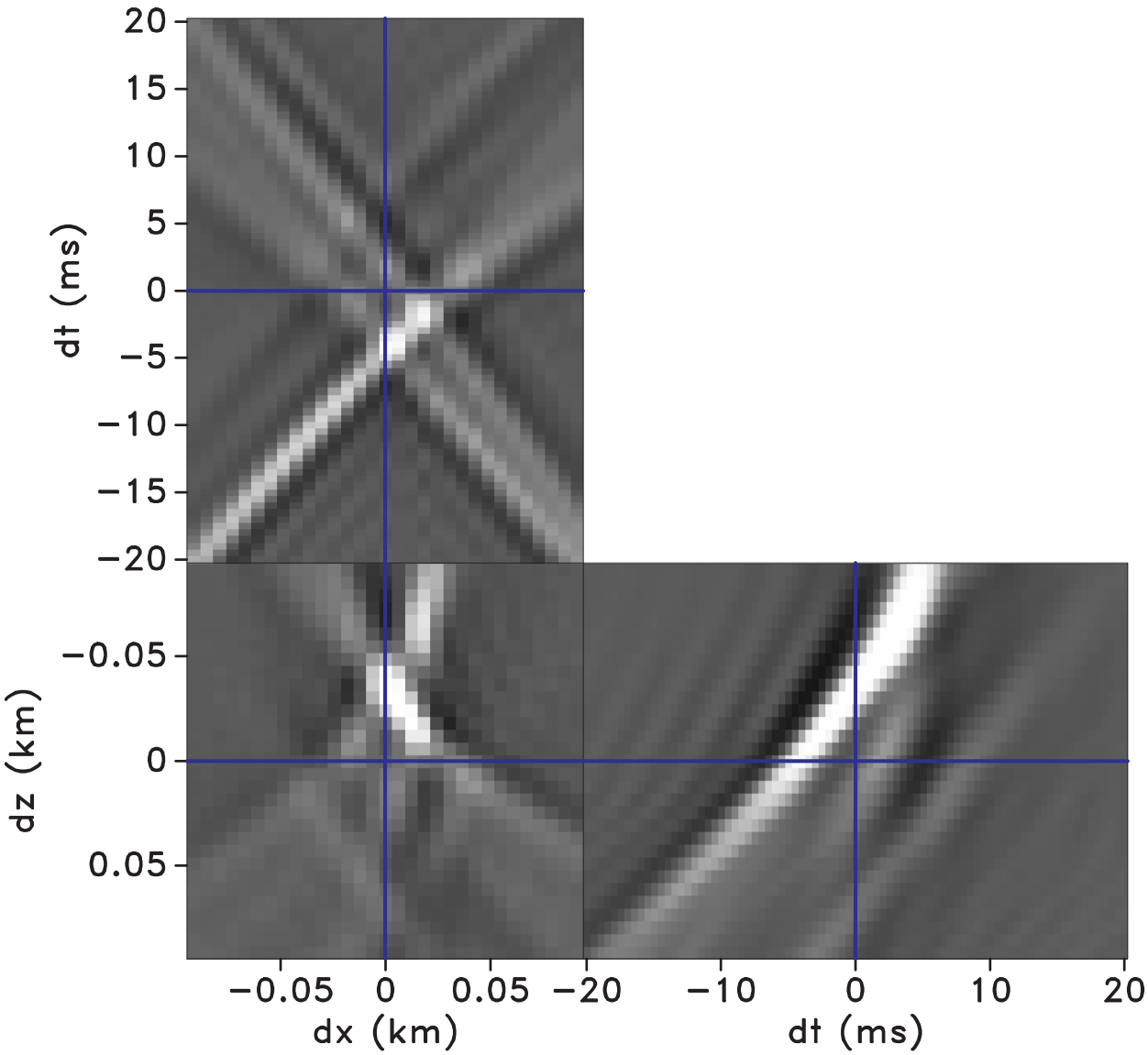


Figure 4.4. Focus obtained using a slow velocity model given the case study geometry shown in Figure 4.1.

Again, the wavefield focus is misplaced by 30 m from the true location, but this time the focus resides above the correct position. Given that the model is smooth, the focus is again smeared vertically and horizontally in space.

Applying an artificial scale to the velocity model, making the velocity model slower and faster than the true model, allows us to understand the effects of velocity of wavefield focusing. The degree of focusing provides information about the resolution of the velocity model, whereas the position of the wavefield focus gives us insight into whether the velocity model is too slow or too fast. The best possible velocity model should be developed before one locates microseismic events, otherwise incorrect placement of focusing leads to incorrect interpretations of fracture geometry.

4.3 Methods for Updating the Velocity Model

Using wavefield focusing as a proxy for velocity model correctness, one may use waveform tomography (Full Waveform Inversion or Waveform Tomography) to improve upon the resolution of the velocity model. Many tomographic techniques, such as the Local Earthquake Tomography (LET) described in Appendix A of this thesis, compare travel-times extracted from a wavefield as a tool to update velocity models. Rather than using just the travel-times, I analyze the entire waveform as a tool for updating velocity models. This way of modeling and velocity updating is based upon the full wave equation rather than travel-times extracted from the wavefields or simulated using ray-tracing. As expressed in Chapter Two of this thesis, picking times on noisy data is challenging. I avoid this challenge by using the two-way wave equation to locate events.

We ultimately want to develop an accurate, high-resolution velocity model so that wavefield focusing is also high-resolution and event picks reside at the correct position in space. An accurate, high-resolution model affords the opportunity to develop a more accurate map of the stimulated fracture network. In order to develop a higher resolution velocity model, we may choose between two tomography techniques. We have the option to

compare the observed and calculated data at the receiver positions and minimize the data residual to update the velocity model. This method is termed data-domain tomography. We may also compare the calculated and ideal wavefield focusing images at a known source location and minimize the image residual to update the velocity model. This method is termed image-domain tomography. For both methods, I illustrate the behavior of the objective function through examples. I construct models by decreasing and increasing the mean slowness. I then plot the data and image residuals with respect to the velocity perturbations, illustrating the behavior of the objective functions.

Waveform tomography directly examines information from the entire wavefield and relates this information to imperfections in the velocity model. One then uses information about the imperfections to be construct a model update or gradient. Once we formulate an objective function, we can iteratively evaluate the gradient numerically using, for example, the Adjoint State Method (Plessix, 2006). The gradient is used to update the model iteratively, and the iteration stops once convergence criteria are met.

In the subsequent sections, I go into the details of both data- and image-domain tomography, illustrating both using the case study model and parameters. I present the residuals in both the data- and image-domain, and I evaluate the characteristics of each objective function as a function of scaled velocity anomalies.

4.3.1 Waveform Tomography: data-domain

Data-domain waveform tomography (Full Waveform Inversion) is an active source inversion method used to update velocity models. It is usually implemented as a local optimization problem that minimizes an objective function defined by data residuals. This method does not simultaneously update the velocity model and locate the source like LET, rather it utilizes known source locations to optimize the velocity model. Data-domain waveform tomography is applicable to microseismic monitoring if there are sources with known locations, absolute timing measurements, and low frequencies. My goal is to understand

the limits and benefits of applying data-domain waveform tomography to the microseismic case.

In exploration seismic, the goal of data-domain tomography is to produce a high-resolution velocity model so that the resulting image of the wavefield is also high-resolution. We need to use a background model that provides enough detailed information (Virieux, 2009) to be able to focus the wavefield. Typically one computes the background model from known or existing velocity models, well logs, core, and/or other *a priori* information. This model, however, must be close to the true velocity model, as local minima and cycle-skipping affect the character of the objective function (Virieux, 2009).

In this technique, we forward model the seismic wavefield $u(\mathbf{x}, t)$ to compute the data $d^{cal}(\mathbf{x}_r, t)$ as a function of receiver position $\mathbf{x_r}$ and time t (Virieux, 2009). Given the calculated data $d^{cal}(\mathbf{x}_r, t)$ and the observed data $d^{obs}(\mathbf{x}_r, t)$ the data residual is given by the following equation:

$$d^{res} = d^{obs}(\mathbf{x}_r, t) - d^{cal}(\mathbf{x}_r, t, m), \tag{4.1}$$

where d^{res} are the data residuals, d^{obs} are the observed data, and the calculated data d^{cal} are a function of the model parameters m. Notice that this data residual is not the same as in equation A.1 used in the LET method; it incorporates the full waveform of the data, not just the time picks. The residuals include all of the waveform information such as the phase, source function, and time. For illustration, Figure 4.5 shows the observed data, calculated data, and data residual given a background model 10% slower than the true model in my case study. A slower model causes the wavefield to propagate slower, producing arrivals in the calculated data later than in the observed data. We expect this timing discrepancy seen in Figure 4.5 because the velocity model is slower than the true model by a factor of 10%. The scaled model does not satisfy the zero-mean assumption, causing the moveout of the events in the calculated data to be different from the observed data. In addition, because the waveforms have an arrival time difference that is larger than the period, the residual contains cycle skipping effects.

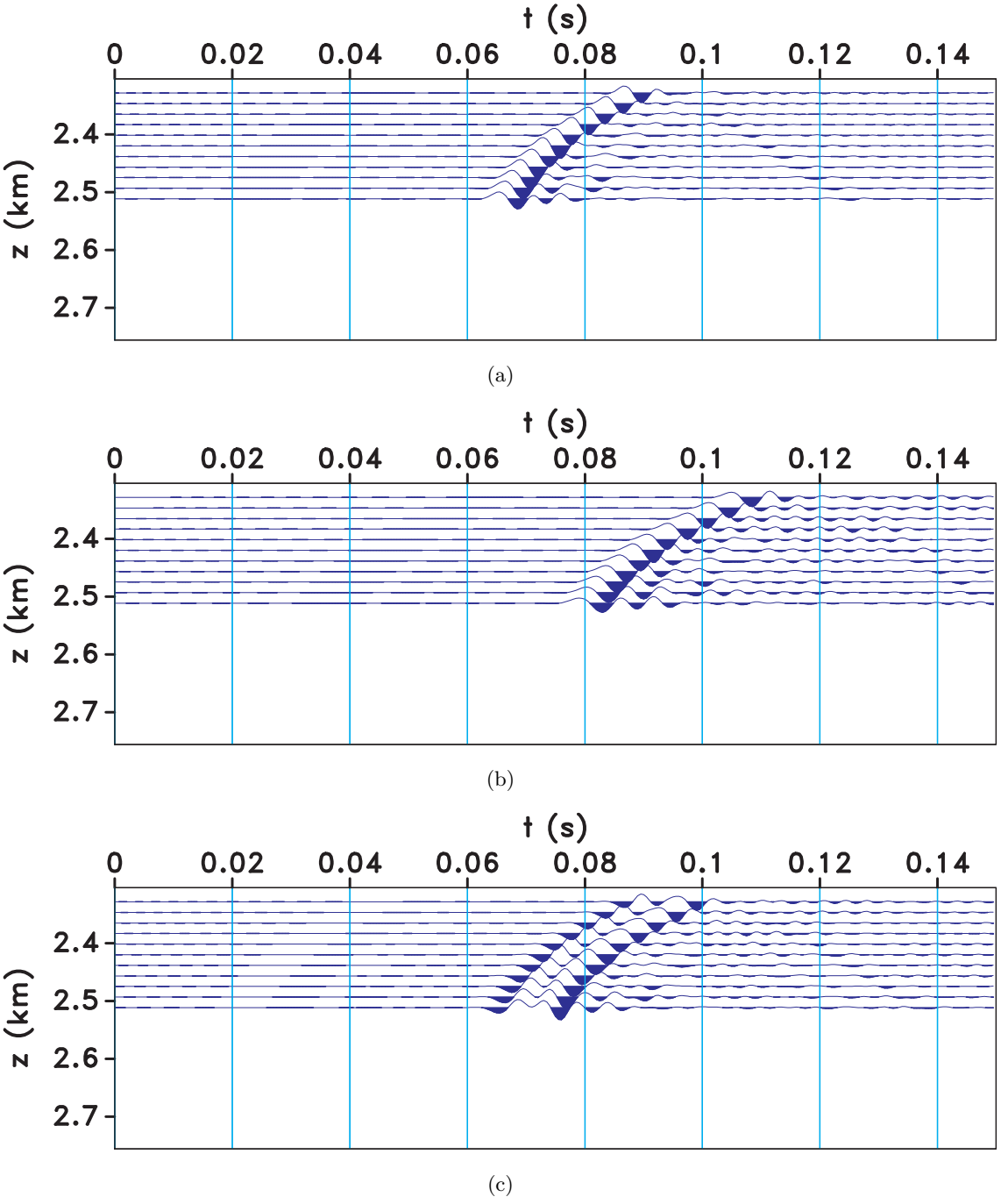


Figure 4.5. A comparison between (a)calculated data d^{cal}, (b) observed data d^{obs}, and (c) the data residual d^{res}. The events in d^{cal} arrive at a time greater than one-wavelength difference from the events in d^{obs}, causing cycle-skipping in d^{res}.

Incorrect velocity is not the only factor affecting the nature of the data residual. The source function of the calculated data must match that of the observed data or the data residuals are not physically correct. If the calculated source function is dissimilar to the observed source function, the calculated and observed phase, frequencies, amplitudes, and/or times are out of sync. This produces a data residual that may contain cycle skipping, inaccurate amplitudes, and other artifacts which result in erroneous gradients and model updates (Virieux, 2009). For microseismic data, even for perforation shots and check shots, we do not know the explicit source function. To make modeling easier, one assumes that a perforation shot is an explosive source since it is often detonated with shaped charges (et. al., 2010a). However, there are many borehole complexities might influence the behavior of the source functions, proving the explosive source assumption false.

Assuming that the starting velocity model is close to the true model, and assuming that the source function is correctly modeled, the goal is to minimize the L2 norm of the data residual, similar to the LET method. The objective function to be minimized is:

$$J(m) = \frac{1}{2} \left\| d^{obs} - d^{cal}(m) \right\|^2, \tag{4.2}$$

where $J(m)$ is the objective function as a function of the model parameters, in this case slowness squared. We use slowness squared as the model to make the inverse problem linear.

To illustrate the objective function in the data-domain, I scale the slowness model in increments of constant 1% slowness perturbations, ranging from a -20% anomaly to a $+20\%$ anomaly. Figure 4.6 shows the computed objective function. One may notice that the objective function oscillates between the maximum and minimum slowness anomalies, producing local minima. If the starting velocity model is not close to the true model, in this case $\pm 5\%$, we converge to a local minimum rather than to the global minimum. On the other hand, if the starting model is close to the true model, the objective function converges to the global minimum at a fast rate. The slope of the objective function is steep within the

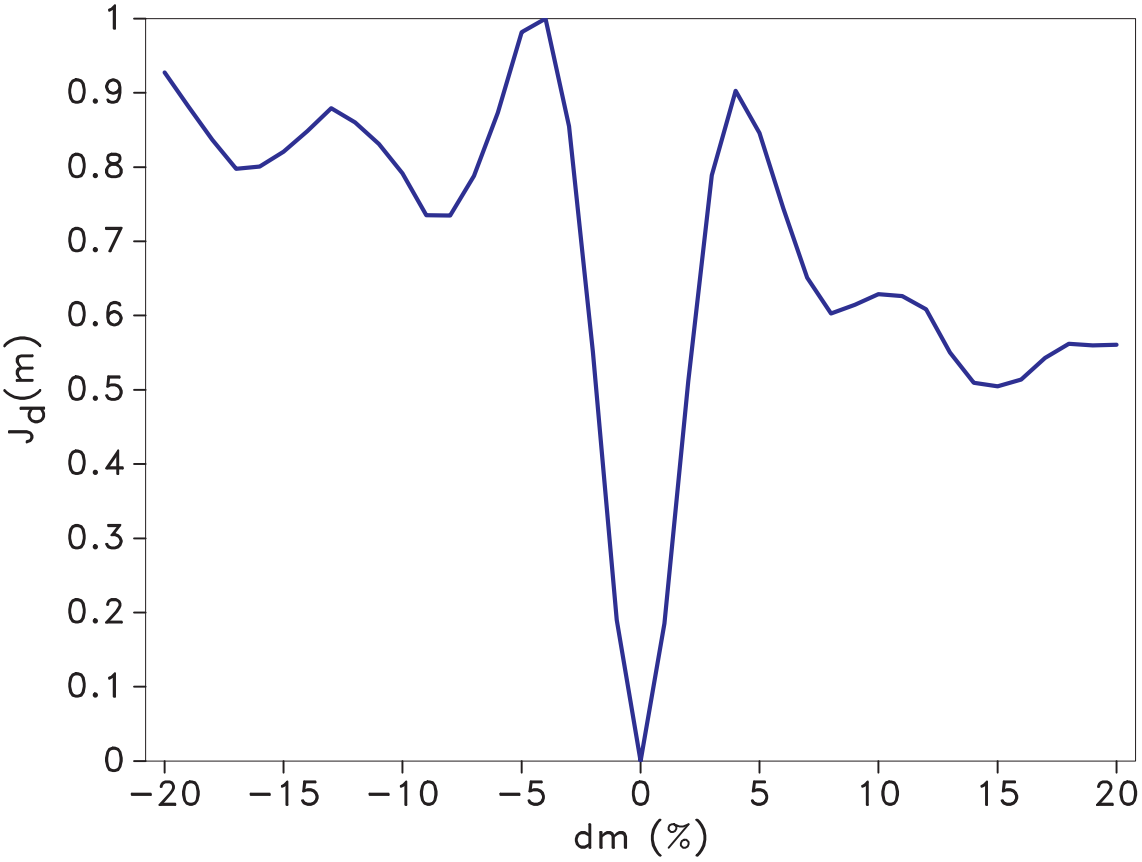


Figure 4.6. Objective function $J(m)$ that minimizes the data residual d^{res} with respect to % scaled slowness anomaly.

near the vicinity (approximately between ±3%) of the true model, thus producing a model with high resolution.

With respect to microseismic monitoring, several issues arise when considering the application of FWI as a tool to update a velocity model. First, the microseismic source is unknown, even with perforation shots. An unknown source function produces an erroneous data residual. Second, the starting model obtained from well logs or other *a priori* information may not be as close to the real velocity model as needed. An incorrect velocity model seeds the inverse problem incorrectly, producing a solution at a local minimum, rather than the global minimum, as illustrated in Figure 4.6. Lastly, microseismic frequencies stretch

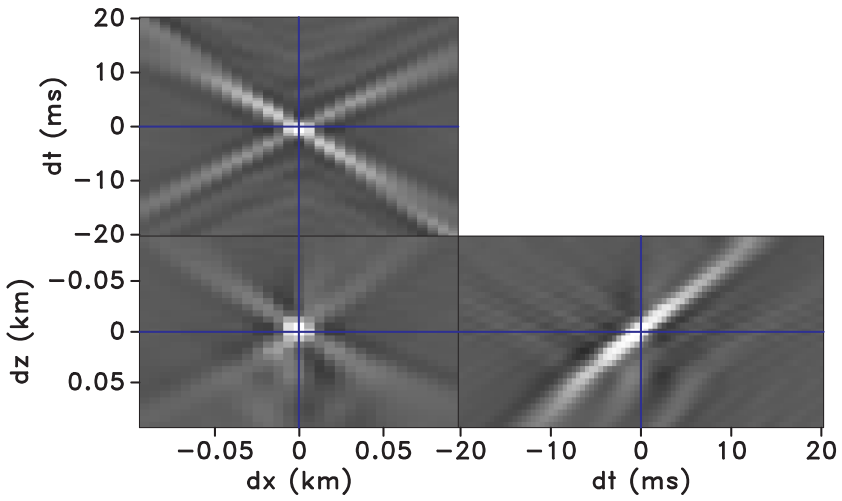
into the kHz range making cycle skipping a real problem when computing the residuals and gradients. All of these issues suggest that FWI is an inappropriate technique to use at present with microseismic velocity model updating unless we know that the starting model is extremely close to the true model.

4.3.2 Waveform Tomography: image-domain

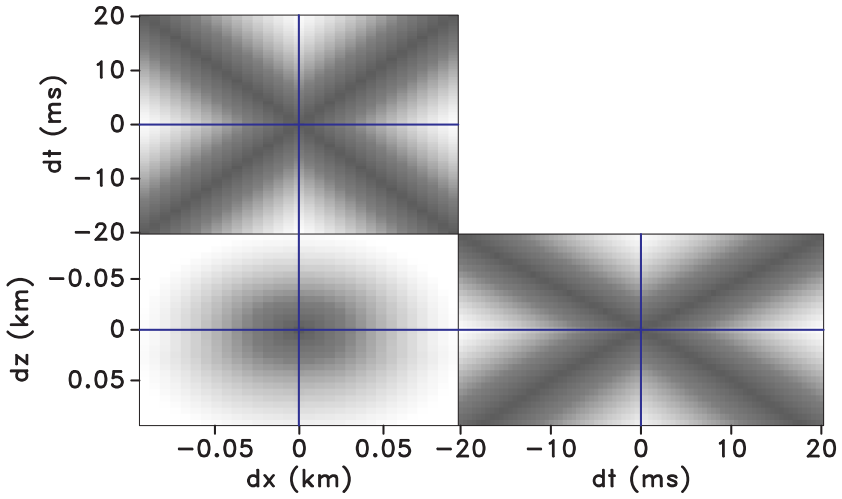
Waveform tomography is not limited to the data-domain. One may implement a similar technique in the image domain and update the model using wavefield focusing instead of data matching. Unlike waveform tomography in the data-domain, tomography in the image-domain theoretically does not rely on the correct estimation of the source function, nor is it affected by cycle skipping. As illustrated in the following examples, the objective function is much flatter and smoother, allowing us to use a starting model that does not necessary have to be close to the true model. We expect that all of these challenges which make data-domain tomography difficult to apply to microseismic imaging, compel us to implement image-domain tomography.

Rather than taking the residual between the forward modeled data and the observed data as described in the data-domain, we compare the wavefield focus to an ideal wavefield focus which we define as a penalty operator (Yang, 2011). The penalty operator theoretically masks the correct portions of the wavefield focus and highlights inconsistencies in the wavefield due to model imperfections (Yang, 2011). Figure 4.7 shows the calculated wavefield focus, the penalty function, and the image residual using the same background model as seen in the data-domain tomography example, a background model which is scaled by a +10% slowness anomaly.

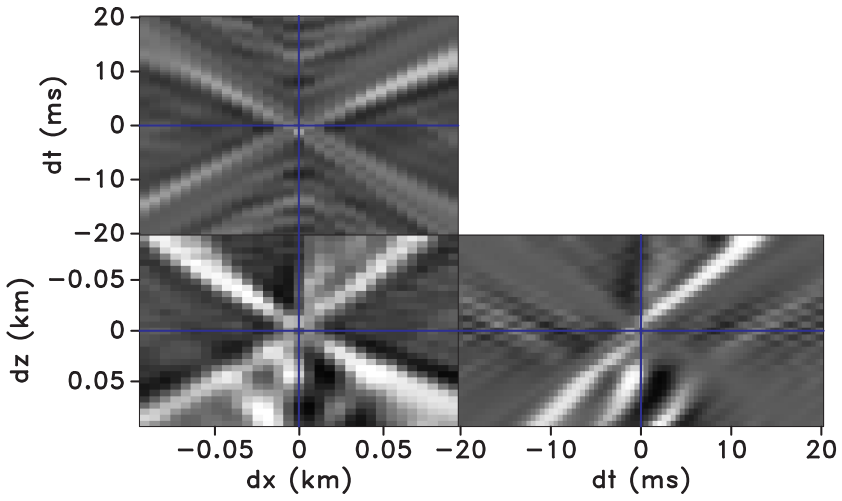
Comparatively, the calculated wavefield focus in the image-domain seen in Figure 4.7, is analogous to the calculated data in Figure 4.5. Rather than observing the wavefield at the receiver locations, we evaluate the entire wavefield at the source location. Similarly, the penalty, or ideal focus in Figure 4.7 is analogous to the observed data seen in Figure 4.5.



(a)



(b)



(c)

Figure 4.7. The (a) calculated wavefield focus, (b) ideal focus, and (c) image residual.

Notice that the ideal focus, or penalty operator, looks a lot like the ideal focus seen in Figure 2.7. Applying the penalty function to the focusing image produces an analogous result to the residual in the data-domain seen in Figure 4.5. Minimizing the residual in Figure 4.7, we construct an objective function that relates the image and the penalty operator:

$$J(m) = \frac{1}{2} \left\| P[R(m)] \right\|^2, \tag{4.3}$$

where $J(m)$ is the objective function as a function of the model parameters m, P is the penalty operator, and $R(m)$ is the image as a function of model parameters. In my case study, the objective function is illustrated in Figure 4.8.

Similar to the data-domain experiment, to produce the objective function I scale the model in increments of 1%, ranging from -20% to $+20\%$, and compute the L2 norm of the synthetic image residual for each model. Notice that the image-domain objective function in Figure 4.8 is much smoother and flatter than the data-domain objective function seen in Figure 4.6. The character of the image-domain objective function implies that the maximum resolution obtainable by this technique is smaller than in the data-domain counterpart, and it also converges at a much slower rate. This comparison allows me to conclude that the image-domain is more robust and is not affected by issues such as cycle skipping due to high frequencies or an unknown source function, but ultimately produces a lower resolution model.

With respect to microseismic monitoring, image-domain tomography is better equipped to handle the issues of unknown source onset time, high frequencies, unknown velocity models, and unknown source functions. Within reason, the starting model seeds the inverse problem, allowing the objective function to converge to a global minimum. However, this global minimum might not provide enough resolution in the velocity model as is desired.

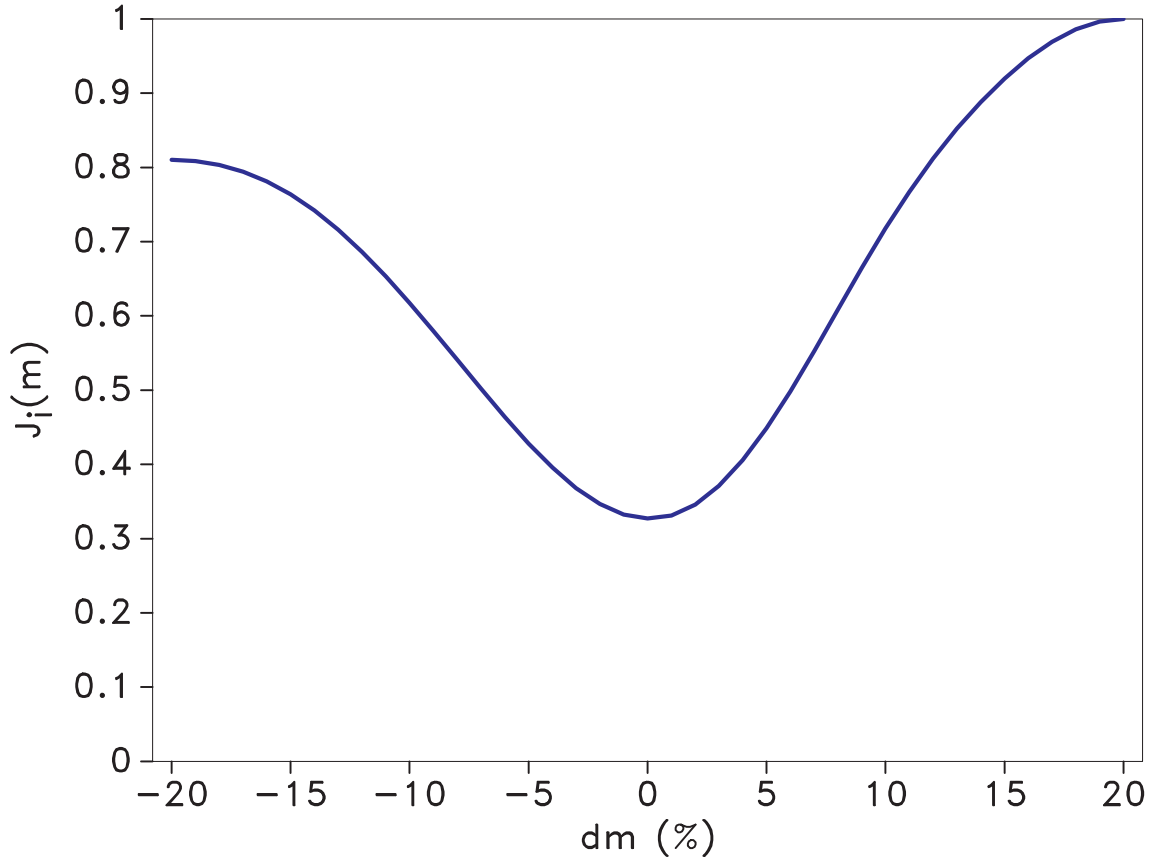


Figure 4.8. Objective function that minimizes wavefield inconsistencies in the image due to an imperfect velocity model.

4.4 Conclusions

Propagating a microseismic wavefield using an incorrect velocity model produces focusing at incorrect locations in space and time. Wavefield velocity inversion techniques may be used to update the microseismic velocity model with the aim of better locating event hypocenters. Data-domain wavefield tomography is hard to implement given the difficulty of estimating the source function and source onset time, and due to the high frequencies present in the data. Image-domain, however, seems to be a more appropriate inversion technique, as it reduces all of the issues present in data-domain tomography. However, image-domain tomography produces lower resolution velocity models compared with the data-domain, as illustrated by both objective functions in my synthetic study. This suggests that a combination of the inverse methods may be more suitable to update the microseismic velocity model. If the starting velocity model is crude, it might be best to optimize the image-domain objective function, first. The velocity model refined through the image-domain tomography method may then be used as the starting model for the data-domain method. This combination of methods would allow for the most accurate, highest resolution velocity model possible.

Chapter 5

CONCLUSIONS AND FUTURE WORK

5.1 Conclusions

Microseismic monitoring has great potential to provide insight into the characteristics of the fracture network activated by hydraulic fracture stimulation. Knowledge of the height, width, and spatial extent of the fractures is valuable information needed for reservoir management and development. Without proper imaging techniques and velocity model calibration, a misinterpretation of the fracture networks is likely, providing misinformation to engineers and management. Throughout this manuscript, I challenge the use of conventional P- and S-picking techniques and advocate the use of wavefield-based methods as a more accurate and more robust alternative.

Realistic microseismic monitoring relies on the use of wellbore and surface arrays of limited aperture to capture enough information to be able to accurately and precisely locate microseisms. In Chapter Two, I explore the effects of a typical microseismic monitor array and advocate for the implementation of larger aperture arrays. Placing receiver arrays on either side of the source, both horizontally and vertically produces a higher degree of focusing in the image. Ideally, this implies that multiple wellbore arrays need to straddle the target formation in depth and should surround the source in x. Using more receivers in an array string as well as deploying a horizontal array also improves the image quality.

The implementation of reverse time imaging has significant challenges, however. Without the knowledge of the onset-time of the source, the source may not be correctly imaged in space or time. An industry tool is available to directly record the onset-time of perforation shots, but may not be readily available to everyone. In Chapter Three, I present a method

used to find the source onset-time when no timing information is available. Using the two-way wave equation, we inspect the wavefield around a known source location in space and time. Theoretically, events exist where wavefields focus. We then shift the wavefield in time so that the focus occurs at time-zero. However, this method is not possible unless we assume that the velocity used to propagate the wavefield has a zero-mean difference from the true velocity model, otherwise the wavefield is misplaced not only by time but also by velocity errors. Through the presentation of synthetic and field examples, I show that the wavefield focusing method works for imaging perforation shots.

Imaging is not accurate unless one develops a high resolution velocity model. Chapter Four discusses the characteristics of wavefield focusing due to an incorrect velocity model. Since waveform tomography naturally compliments the use of wave-equation modeling, I investigate the applicability of waveform tomography in both the data- and image-domain. Image-domain tomography is less sensitive to unknown parameters such as the starting velocity model and source functions, and is more robust in the presence of high frequencies natural to microseismic events. However, data-domain tomography has the potential to produce a much higher resolution velocity model.

5.2 Suggested Future Work

After much discussion on the negative effects of a limited array aperture and an incorrect velocity model have on the ability to focus the microseismic wavefield, I conclude that future work is needed in these areas to improve the overall quality of microseismic event locations.

A field test should be conducted where the aperture of the monitor array is significantly enlarged. I recommend that there are multiple arrays which straddle the target formation in x and z. The deployment of a horizontal array, either on the surface or in a wellbore, in conjunction with the wellbore arrays has the potential of improving the resolution of wavefield focus. In addition, an economic analysis is beneficial to establish an aperture

threshold of where the costs of extending the aperture outweigh the benefits.

Beyond the improvements in the acquisition aperture, research should be conducted on the possibility of combining inversion techniques from both the data- and image-domain tomography methods. Image-domain tomography might prove to be the best starting velocity inversion technique. Data-domain tomography may then use the velocity model produced in the image-domain to refine the velocity to the highest resolution possible.

REFERENCES

Abel, S. Coffin, Y. Hur S. Taylor. 2011. An analytic model for microseismic event location estimate accuracy. *First Break*, **29**, 99–107.

Artman, I. Podladtchikov, B Witten. 2010. Source location using time-reverse imaging. *Geophysical Prospecting*, **58**, 861–873.

Backus, G. 1962. Long-Wave Elastic AnisotropyProducedby Horizontal Layering. *Journal of Geophysical Research*, **67**(11), 4427–4440.

Bardainne, E. Gaucher. 2010. Influence of models on seismic-event localization. *Geophysical Prospecting*, **58**, 739–753.

Bose, S, Valero, H, Liu, Q, Shenoy, R G, & Ounadjela, A. 2009. An Automatic Procedure to Detect Microseismic Events Embedded in High Noise. *SEG Technical Program Expanded Abstracts*, 1537–1541.

Drew, D. Leslie, P. Armstrong G. Michaud. 2005. Automated Microseismic Event Detection and Location by Continuous Spatial Mapping. *SPE*.

Eisner, L. 2010. Comparison of surface and borehole locations of induced seismicity. *Geophysical Prospecting*, **58**(5), 809–820.

et. al., Bell. 2010a. Advances in Perforating Technology Continue. *Journal of Petroleum Technology*, 23–25.

et. al., Godwin. 2011. Automatic microseism location by full-waveform triangulation. *EAGE*, 23–26.

et. al., Kissling. 1994. Initial reference models in local earthquake tomography. *Journal of Geophysical Research*, **99**, 19,635–19,646.

et. al., Murer. 2010b. Why Monitoring With a Single Downhole Microseismic Array May Not Be Enough: A Case For Multiwell Monitoring of Cyclic Steam in Diatomite. *SPE*.

Gajewski. 2009. Influence of models on seismic-event localization. *Geophysics*, **74**(5), WB55–WB61.

Grechka, V. 2010. Data-acquisition design for microseismic monitoring. *SEG, The Leading Edge*, **29**(3), 278–282.

Hayles, Kristin, Horine, Robert L., Checkles, Steve, & Blangy, J. P. 2011. Comparison of microseismic results from the Bakken formation processed by three different companies: Integration with surface seismic and pumping data. *SEG Technical Program Expanded Abstracts*, **30**(1), 1468–1472.

Hubbert, M. 1957. Mechanics of Hydraulic Fracturing. *SPE*, **210**, 153–168.

Lindsay, R., & Koughnet, R. V. 2001. Sequential Backus Averaging: Upscaling well logs to seismic wavelengths. *The Leading Edge*, **20**(2), 188–191.

Maxwell, & Urbancic. 2001. The role of passive microseismic monitoring in the instrumented oil field. *SEG, The Leading Edge*, **20**(6), 636–639.

Plessix, R.E. 2006. A review of the adjoint-state method for computing the gradient of a functional with geophysical applications. *Geophysics Journal International*, **167**, 495–503.

Rentsch, S. 2007. Fast location of seismicity: A migration-type approach with application to hydraulic-fracturing data. *Geophysics*, **72**(1), S33–S40.

Thurber, C. 1992. Hypocenter-velocity structure coupling in local earthquake tomography. *Physics of the Earth and Planetary Interiors*, **75**, 55–62.

Tiwary, D. 2009. Comparison of Seismic Upscaling Methods: From Sonic to Seismic. *Geophysics*, **74**(2).

Uhl, Wright, Davis Ward Warpinski. 2006 (2). *Microseismic Fracture Mapping using seismic source timing measurements for velocity calibration.*

Virieux, Operto. 2009. An overview of full-waveform inversion in exploration geophysics. *Geophysics*, **74**(6), WCC1–WCC26.

Warpinski et. al., R.B. Sullivan, J.E. Uhl C.K. Waltman S.R Machovoe. 2005. Improved Microseismic Fracture Mapping Using Perforation Timing Measurements for Velocity Calibration. *SPE*, **10**(1), 14–23.

Xuan, R., Sava P. 2010. Probabilistic microearthquake location for reservoir monitoring. *Geophysics*, **75**(3).

Yang, Sava. 2011. Image-domain waveform tomography with two-way wave-equation. **Proceedings from the 81st Annual International Meeting**.

Zimmer, Ulrich. 2012. Microseismic design studies. **76**(6).

APPENDIX A

A.1 Local Earthquake Tomography

LET is common practice in earthquake seismology today, simultaneously locating earthquake hypocenters and updating velocity models of the Earth. The arrival time of a wavefront is a nonlinear function of source-receiver geometry and the velocity field. In earthquake seismology the only parameters typically known are the relative arrival times of the seismic wavefront between receivers and the absolute geometry and locations of the receivers. The hypocenter and onset time of the source and the velocity field are all unknowns (et. al., 1994; Thurber, 1992). This is no different from microseismic: neither the velocity field nor onset time of the source are known. For both earthquake seismology and microseismic monitoring, one makes an educated guess of the model parameters (hypocenter, source onset time, and velocity) using *a priori* information. One then devleopes a one-dimensional starting velocity model using information such as well logs, core, or previously constructed velocity models. Once a velocity model is constructed, one makes an initial guess of the location of the hypocenter. Triangulation or ray theory are common in locating hypocenters.

Triangulation operates by calculating spheres on which hypocenters may reside (also referred to as isochrons or spheres of similar time), given the differences in arrival of P- and S-phases, the velocity model, and the location of each receiver. A sphere is calculated for each receiver, and where all spheres intersect is the location of the earthquake hypocenter.

The initial hypocenter guess may also be determined by constructing a grid containing model parameters. Travel times are then calculated from the receiver locations to each point in the grid using ray theory (Thurber, 1992). The back-projected takeoff angle (dip

and azimuth) of the ray is calculated from the polarizations of the recorded data at the receivers. (A hodogram, or plot of particle motion with respect to time, provides sufficient information about the takeoff angle required to initialize the path integral used in ray theory.) The point in the model parameter grid where the calculated travel times best match the observed travel times is considered the initial hypocenter location.

Once an initial estimate of the travel time is calculated, given the first-guess hypocenter location and starting velocity model, the goal is to minimize the residuals between the observed and calculated travel times:

$$r_k^i = T_k^{i\,obs} - T_k^{i\,cal}, \tag{A.1}$$

where r_k^i is the travel time residual.

A customary approach to solving this inverse problem is to minimize the travel time residuals by applying an iterative damped, regular, and/or weighted least squares algorithm. The travel time residuals may be expressed as a function of source-receiver geometry and velocity. Perturbing the hypocenter location and the velocity model by certain amounts will change the travel time calculation. This expression allows for the inversion of both hypocenter locations and velocity values.

The process of simultaneously locating earthquake or microseismic hypocenters and updating the velocity model is a relatively straightforward problem. In fact, LET is one of the most widely cited microseismic processing techniques seen in literature today. LET is a valuable tool, however, there are significant challenges that must be recognized when applying LET to microseismic data.

LET was originally designed for global- and regional-scale earthquake location and tomography problems. The monitoring arrays inherently contain a large aperture, and the waveforms are extremely low-frequency compared to that seen in microseismic monitoring. In addition, one may reference many earthquake hypocenters and crustal velocity models in

earthquake catalogues and available to the public. Between the large array aperture, low frequencies, and extensive database, one has more information available to locate earthquakes than when locating microseismic hypocenters.

Microseismic monitoring, both surface and borehole, have very limited array apertures compared to earthquake monitoring arrays. Limited aperture makes both ray theory, triangulation, and migration all difficult tasks to locate events accurately. Oftentimes events are smeared the vertically or horizontally. In addition, the waveforms are high-frequency and oftentimes the data are proprietary and not available to the public, allowing for no cross-check between previously catalgued data.

Typically, the starting velocity model includes information from well logs, core, and/or geologic sections. As this information is one-dimensional, one must further calibrate the velocity model (Bardainne, 2010). Applying the well established LET method to microseismic, one minimizes the arrival time difference between the forward modeled arrival times and the observed data arrival times to obtain an optimized velocity model. One uses the difference between the arrival times in an inversion or calibration algorithm to update the velocity model until the inversion reaches an optimized solution (Thurber, 1992). LET, however, is limited to the ability of picking P- and S-arrivals as well as identifying, through hodograms, the angle at which the rays are incident at the receiver locations. In data overwhelmed by noise, the implementation of LET is not ideal for locating microseismic events (Gajewski, 2009; Drew, 2005).

APPENDIX B

B.1 Backus Averaging

Sonic velocity logs are a vital source of information in geophysical analysis. They are the starting point for many geophysical methods such as microseismic analysis, tying wells to seismic, and the computation of various synthetic seismograms. Sonic logs, however, are recorded at frequencies much higher than what are seen in seismic methods. In order to be able to use sonic logs on a seismic scale, it is necessary to upscale them. There are many different methods of well log upscaling that exist, but only a few that are appropriate for upscaling well logs. The goal is to upscale the sonic logs without changing the properties seen at seismic wavelengths. This appendix presents a discussion on the Backus Averaging method and its benefits and drawbacks.

Upscaling sonic logs to seismic frequencies while preserving the original formation properties is imperative for modeling accurate seismic responses of formations. High-frequency sonic logs can record frequencies up to 15kHz, whereas seismic frequencies range between approximately 8Hz and 100 Hz (Tiwary, 2009). There exist many methods for upscaling well logs: frequency filtering, simple smoothing algorithms, and more complex upscaling schemes. Upscaled well logs are dependent upon original formation properties: layer thickness, acquisition bandwidth, and formation velocities (Lindsay & Koughnet, 2001) Given the variability in formations, to preserve the original formation properties, it it is common to implement Sequential Backus Averaging.

B.1.1 Well Log Upscaling Methodology

Backus Averaging, first developed by George E. Backus in 1962, averages the elastic moduli and bulk density of a finely layered medium, and outputs properties that look like those of a single, averaged, thick medium. The averaging algorithm is based on the effective medium theory: it is implemented sequentially in small depth increments, where the sizes of the depth increments are much smaller than a seismic wavelength. In other words, finely layered media can be regarded as an *effective homogeneous medium*. Backus Averaging, in its simplest form, assumes each thin layer to be isotropic and horizontally infinite, defined by either bulk moduli or Lam*é* parameters. In this paper, Lam*é* parameters are used. From these thin layers, a volume-weighted average of the elastic properties is computed. Shear and compressional velocity, along with bulk density are then computed from the volume-weighted elastic moduli (Backus, 1962).

The calculated shear and compressional velocities are dependent upon the ratio of the dominant measurement wavelength to the thickness of the layers in the medium. When the wavelength is large compared to the layer thickness, the velocity is given by an average of the elastic properties of the layers (Tiwary, 2009).

Applied to well logs, depth is transformed to two-way time via this expression: $T = 2 * (dt/Vp)$, where T is two-way time, dt is the time sampling rate, and Vp is the compressional velocity log. In this case, the sampling rate is chosen to be 4ms. The two-way time is calculated for every depth interval (every 0.5 ft or 0.1542 m). Once enough two-way time is accrued, the Lam*é* parameters λ and μ are computed for each of the thin layers using the following equation:

$$\mu_i = \rho_i V_{s_i}^2 \lambda_i = \rho_i V_{p_i}^2 - 2\mu_i, \tag{B.1}$$

where i is the index of each thin layer (now expressed in two-way time), Vp is compressional velocity, and Vs is shear velocity.

Using the calculated Lamé parameters at every thin layer, stress and strain are weighted time averaged to compute the elastic constants in the stiffness tensor (Backus, 1962):

$$C_{ijkl} = \begin{bmatrix} A & B & F & 0 & 0 & 0 \\ B & A & F & 0 & 0 & 0 \\ F & F & C & 0 & 0 & 0 \\ 0 & 0 & 0 & D & 0 & 0 \\ 0 & 0 & 0 & 0 & D & 0 \\ 0 & 0 & 0 & 0 & 0 & M \end{bmatrix}. \tag{B.2}$$

From the weighted time averaged stiffness tensor, shear and compressional velocities are *backed out* using the expressions in the following equation:

$$V_p = \sqrt{\frac{A}{\langle\rho\rangle}} = \sqrt{\frac{C_{11}}{\langle\rho\rangle}} V_s = \sqrt{\frac{D}{\langle\rho\rangle}} = \sqrt{\frac{C_{44}}{\langle\rho\rangle}} \rho = \langle\rho\rangle, \tag{B.3}$$

where $\langle\rho\rangle$ is the time-weighted average density (Backus, 1962). C_{11} and C_{44} are A and D, respectively, of the stiffness tensor see in equation B.3. Using Lamé's parameters, C_{11} and C_{44} are defined using the expressions (Backus, 1962):

$$C_{11} = A = \langle\frac{4\mu(\lambda+\mu)}{\lambda+2\mu}\rangle + \langle\frac{1}{\lambda+2\mu}\rangle^{-1}\langle\frac{\lambda}{\lambda+2\mu}\rangle^2 C_{44} = D = \langle\frac{1}{\mu}\rangle^{-1}, \tag{B.4}$$

where $\langle . \rangle$ denotes a time-weighted average.

Once the compressional and shear velocity logs as well as the density log are backed out from the time-weighted averaged parameters, the time axis may then be transformed back to depth. The number of samples in the output logs is dramatically reduced and the logs now have the desired frequencies present (for the case of $dt = 4$ ms, the logs will have 125 Hz present).

It is important to take note that the method of Backus Averaging is only valid under certain assumptions. The material which is averaged must be normal to the incident wave,

isotropic, and thinly layered. Wavefronts are assumed to be parallel to and much longer than the length of the bedding. In addition, P-wave attenuation is assumed to be zero. In other words, if the formation contains fluids, such as attenuation and dispersion, intermediate frequency effects are ignored (Tiwary, 2009). More complicated forms of Backus Averaging exist which include non-normal incident ray-paths and fluid effects. However, the mathematics are beyond the scope of the discussion in this appendix.

B.1.2 Case Study Results

The form of Backus Averaging presented in this appendix band-limits the well logs while preserving the original petrophysical properties. It upscales the well logs so that the resolution, with respect to the petrophysical properties of the elastic material, is the same as seen in seismic . The following figure shows an example of a real compressional velocity well log (black) and it's corresponding Backus Averaged equivalent (blue).

Theoretically, Backus Averaging is the most appropriate method for upscaling well logs to seismic frequencies. Mathematically, it preserves the original petrophysical properties of the formation by incorporating effective medium theory.

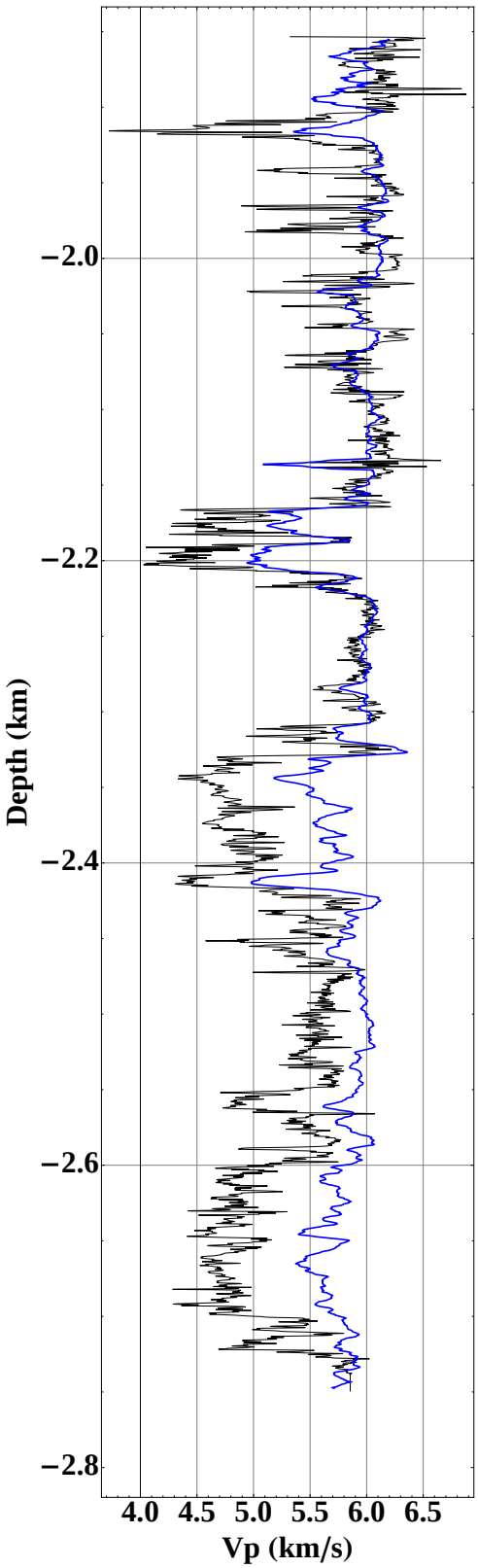


Figure B.1. Vp well log (black), Backus Averaged Vp (blue) The vertical axis is depth in km and the horizontal axis is velocity in km/s.